Monthly Notices
of the
ROYAL ASTRONOMICAL SOCIETY

MNRAS **459,** 3326–3348 (2016)
Advance Access publication 2016 April 5

doi:10.1093/mnras/stw777

The quiescent phase of galactic disc growth

Michael Aumer,* James Binney and Ralph Schönrich
Rudolf Peierls Centre for Theoretical Physics, 1 Keble Road, Oxford OX1 3NP, UK

Accepted 2016 March 30. Received 2016 March 30; in original form 2016 February 3

ABSTRACT

We perform a series of controlled *N*-body simulations of growing disc galaxies within non-growing, live dark matter haloes of varying mass and concentration. Our initial conditions include either a low-mass disc or a compact bulge. New stellar particles are continuously added on near-circular orbits to the existing disc, so spiral structure is continuously excited. To study the effect of combined spiral and giant molecular cloud (GMC) heating on the discs, we introduce massive, short-lived particles that sample a GMC mass function. An isothermal gas component is introduced for a subset of the models. We perform a resolution study and vary parameters governing the GMC population, the histories of star formation and radial scale growth. Models with GMCs and standard values for the disc mass and halo density provide the right level of self-gravity to explain the age–velocity dispersion relation of the solar neighbourhood (Snhd). GMC heating generates remarkably exponential vertical profiles with scaleheights that are radially constant and agree with observations of galactic thin discs. GMCs are also capable of significantly delaying bar formation. The amount of spiral-induced radial migration agrees with what is required for the metallicity distribution of the Snhd. However, in our standard models, the outward-migrating populations are not hot enough vertically to create thick discs. Thick discs can form in models with high baryon fractions, but the corresponding bars are too long, the young stellar populations too hot and the discs flare considerably.

Key words: methods: numerical – Galaxy: disc – Galaxy: kinematics and dynamics – Galaxy: structure – galaxies: evolution – galaxies: spiral.

1 INTRODUCTION

The vertical profile of our Galaxy in the solar neighbourhood (Snhd) can be closely fitted by the sum of two exponentials with scaleheights of $h_{z,\rm thin} \sim 300$ pc and $h_{z,\rm thick} \sim 900$ pc (Gilmore & Reid 1983; Jurić et al. 2008). Jurić et al. (2008) found that both thin and thick components could be characterized by exponential radial profiles, with the thick component having a larger scalelength than the thin component. Many external disc galaxies also show vertical profiles that can be decomposed into thin and thick components (Yoachim & Dalcanton 2006), with the thick component having a radial scalelength that is similar to, or slightly larger than, the scalelength of its thin counterpart.

In the solar cylinder, the thick component contributes ∼30 per cent of the local stellar mass surface density, and its stars tend to have larger random velocities, higher ages, lower metallicities and higher α-element abundances (Bensby, Feltzing & Lundström 2003). In a plot of [α/Fe] versus [Fe/H], two sequences can be identified: a 'normal' or 'low-α' sequence, which starts around [Fe/H] ~ -0.6 with a small slope, and a 'high-α' sequence, which is nearly flat at low [Fe/H] and then bends more steeply downwards to join the low-α sequence around [Fe/H] ~ 0.2. Bovy et al. (2012b) used data from the SEGUE survey to argue that the vertical velocity dispersion of stars varies continuously with chemistry, and that signs of a thin/thick-disc dichotomy are an artefact of selection functions. However, Nidever et al. (2014) and Hayden et al. (2015) found well-defined low- and high-α abundance sequences in the ([Fe/H], [α/Fe]) plane of the APOGEE survey. While it is tempting to infer two distinct populations from a bimodality in [α/Fe], Schönrich & Binney (2009a,b, hereafter SB09a,b) have shown that such a bimodality is a natural consequence of chemical evolution time-scales.

The high-α sequence dominates larger altitudes in the disc, but its importance diminishes towards larger radii. This observational finding has led to the conclusion that the α-rich component of the Milky Way (MW) has a comparably shorter scalelength (Bensby et al. 2011; Bovy et al. 2012a; Cheng et al. 2012). This fading of the thick high-α component seems to contradict the long photometric thick-disc scalelength found by Jurić et al. (2008) and the lack of evidence of a change in the vertical profile as a function of radius both in our Galaxy and in external disc galaxies (van der Kruit & Searle 1982; Comeron et al. 2011). One possibility is that low-α populations flare with increasing radius and take the role of the thick component in the outer disc (see e.g. Minchev et al. 2015).

* E-mail: Michael.Aumer@physics.ox.ac.uk

The vertical scaleheight of a stellar population in a given galactic potential is determined by its vertical velocity dispersion. If we group nearby stars by age, the velocity dispersion of the group increases with age (Strömberg 1946; Parenago 1950; Wielen 1977). This phenomenon has been inferred also for external galactic discs (Beasley et al. 2015 for M33; Dorman et al. 2015 for M31). However, for Snhd stars this increase appears to be continuous with age and does not indicate a thin–thick bimodality (Aumer & Binney 2009; Holmberg, Nordström & Andersen 2009).

Currently, stars are born very close to the plane with small velocity dispersions, but over time fluctuations in the Galaxy's gravitational field cause stars to diffuse from the near-circular orbits of their birth to more eccentric and inclined orbits, with the consequence that the velocity dispersion of each coeval group of stars steadily increases. It is possible that *all* disc stars were born on nearly circular orbits, but it is also possible that at early times the young Galaxy's gravitational field fluctuated so strongly that even dense gas could not settle to circular orbits, so stars had significant random velocities at birth. A major goal of this paper is to investigate the possible genesis of thick-disc stars assuming no significant external perturbation throughout the era in which nearly all disc stars formed.

Fluctuations in the gravitational field that accelerate stars can arise in several ways. Spitzer & Schwarzschild (1953) suggested that an important source of fluctuations is giant gas clouds. The subsequent discovery of giant molecular clouds (GMCs) with masses $M_{\rm GMC} \sim 10^{5-7}\,{\rm M}_\odot$ vindicated this suggestion. Barbanis & Woltjer (1967) showed that spiral structure can be a significant source of fluctuating gravitational field, provided it has either a very high density contrast or is of transient and recurring nature. Stars can also be heated by merging satellite galaxies (Gerhard & Fall 1983; Toth & Ostriker 1992; Velazquez & White 1999).

Another key ingredient in the evolution of disc galaxies is bars. In today's Universe around 70 per cent of all disc galaxies, including the MW (Binney et al. 1991), have stellar bars at their centres (Eskridge et al. 2000). Bars have been shown to contribute to the radial and vertical heating in disc galaxies (Saha, Tseng & Taam 2010) and to provide a mechanism for the radial migration of stars (Friedli, Benz & Kennicutt 1994; Minchev & Famaey 2010). Bars are believed to be a natural outcome of the evolution of dynamically cold galactic discs (e.g. Miller & Smith 1979). However, observations of galaxies at redshifts between 0 and 1 have revealed that the fraction of bars was significantly lower several Gyr ago (Sheth et al. 2008).

Although it is generally believed that a combination of heating processes mentioned above can explain the thin-disc age–velocity dispersion relation (AVR), the origin of the thick disc is still heavily debated. Two key questions are: (1) Did thick-disc stars form in a thin disc which was subsequently heated, or did they form with large random velocities in a turbulent gas disc (Bournaud, Elmegreen & Martig 2009; Forbes, Krumholz & Burkert 2012)? (2) If they formed in a thin disc is an external perturber required to endow them with their present random velocities, or could these have arisen through internal secular processes, such as scattering off the bar (Minchev & Famaey 2010) and GMCs followed by radial migration (Sellwood & Binney 2002) of stars from the hot inner disc to the cooler outskirts (SB09b)?

In this paper, we seek to understand whether double-exponential vertical profiles of disc galaxies can arise purely from secular evolution, i.e. from heating by GMCs and by structures such as bars and spirals, which inevitably occur in a growing disc galaxy (Sellwood & Carlberg 1984; Carlberg & Sellwood 1985). As spiral heating is expected to contribute little to the vertical heating (see Martinez-Medina et al. 2015 for a recent confirmation with modern isolated disc simulations), our focus here is on GMCs, bars and the outward transport of hot populations through radial migration.

To study these heating processes, usually idealized, isolated models have been used. Unfortunately, the majority of these models do not at the same time include all the ingredients, which have been implicated in disc heating: growing discs with multiple coeval populations, recurring spiral structure with evolving properties, a bar, radial migration, and GMCs that at early times each contain a bigger fraction of the total disc mass than they do today.

Cosmological, hydrodynamical simulations of the formation of disc galaxies do, in principle, contain all these items and have recently also become capable of producing disc galaxies with realistic structural parameters and star formation histories (SFHs; e.g. Aumer et al. 2013; Marinacci, Pakmor & Springel 2014) and have also been used to study disc heating (House et al. 2011; Bird et al. 2013; Martig, Minchev & Flynn 2014). However, the uncertainties regarding the proper modelling of hydrodynamics and 'sub-grid' physics are still substantial (e.g. Scannapieco et al. 2012), and simulations with a resolution of <100 pc as desired are still very costly, which prevents large sets of such models. Models of idealized disc galaxies growing from the cooling of hot gas in an idealized and isolated or cosmological dark matter halo (Aumer & White 2013; Roškar, Debattista & Loebman 2013) are more easily accessible for the problems considered here, but concerns regarding hydrodynamics and sub-grid models and their effect on young stellar populations in the simulations remain. For example, House et al. (2011) discuss how birth velocity dispersion depends on resolution and the assumed star formation (SF) prescription.

We therefore pursue a different, complementary approach, which allows us to study disc heating with *N*-body simulations. We return to the approach pioneered by Sellwood & Carlberg (1984), but used in only a few papers since then [notably the study by Berrier & Sellwood (2015) of the emergence of exponential surface density profiles from arbitrary angular-momentum distributions of infalling matter]. In this approach, particles representing stars, and possibly gas and GMCs, are continuously added on near-circular orbits. Spiral structure and bars are naturally excited in the disc, and they both accelerate the stars and cause them to migrate radially. We analyse our final models to determine how they compare with observational diagnostics of disc heating in the MW. Given the need to use arbitrary prescriptions for sub-grid physics in full hydrodynamical simulations of disc growth, the models are no less rigorous than full simulations, and, since they are computationally cheaper, we can run large numbers of models and gain a reasonable understanding of how a growing disc can evolve in isolation.

In this paper, we (i) present a set of novel numerical simulations of growing galaxies and explain how they were set up and run, and (ii) give an overview of the most important lessons learnt from these simulations. More detail will follow in papers on particular aspects of galactic growth, such as the AVR for nearby stars and its connection to the underlying heating laws, the distribution function of the dark halo, the impact of spiral structure on star surveys or the details of radial migration processes. The structure of the paper is as follows: Section 2 defines the simulations. Section 3 justifies our modelling strategy by showing insensitivity to the adopted initial conditions (ICs) and adequate resolution. Section 4 demonstrates the fundamental role played by GMCs, explores the more minor role played by space-filling interstellar gas, and discusses heating and radial migration within discs. A key result of this section, in which the disc mass and the structure of the dark halo are in line

Table 1. An overview over the different models and their parameters. Column 1: IC name; column 2: total IC mass $M_{\rm tot}$; column 3: total baryonic IC mass $M_{\rm b,i}$; column 4: total gas IC mass $M_{\rm gas,i}$; column 5: number of DM particles $N_{\rm DM}$ in IC; column 6: number of baryonic particles $N_{\rm b,i}$ in IC; column 7: concentration parameter for IC DM halo, $c_{\rm halo}$; column 8: IC DM halo scalelength $a_{\rm halo}$ column 9: IC radial disc scalelength $h_{R,\rm disc}$; column 10: IC vertical disc scaleheight $z_{0,\rm disc}$; column 11: IC bulge scalelength $a_{\rm bulge}$; column 12: gravitational softening length for DM particles, $\epsilon_{\rm DM}$; column 13: gravitational softening length for baryonic particles, $\epsilon_{\rm b}$.

(1) Name	(2) $M_{\rm tot}$ ($10^{12}\,{\rm M}_\odot$)	(3) $M_{\rm b,i}$ ($10^{9}\,{\rm M}_\odot$)	(4) $M_{\rm gas,i}$ ($10^{8}\,{\rm M}_\odot$)	(5) $N_{\rm DM}$	(6) $N_{\rm b,i}$	(7) $c_{\rm halo}$	(8) $a_{\rm halo}$ (kpc)	(9) $h_{R,\rm disc}$ (kpc)	(10) $z_{0,\rm disc}$ (kpc)	(11) $a_{\rm bulge}$ (kpc)	(12) $\epsilon_{\rm DM}$ (pc)	(13) $\epsilon_{\rm b}$ (pc)
Y	1	5	–	5000 000	500 000	9	30.2	1.5	0.1	–	134	30
Z	1	10	–	5000 000	1000 000	9	30.2	1.5	0.5	–	134	30
A	1	10	–	5000 000	1000 000	9	30.2	1.5	0.8	–	134	30
E	1	15	–	5000 000	1500 000	9	30.2	2.5	1.2	–	134	30
EHR	1	15	–	15 000 000	4500 000	9	30.2	2.5	1.2	–	90	20
S	1	2	–	5000 000	200 000	9	30.2	1.5	0.1	–	134	30
YLH	1	5	–	1000 000	500 000	9	30.2	1.5	0.1	–	200	30
YLR	1	5	–	2000 000	200 000	9	30.2	1.5	0.1	–	170	30
YHH	1	5	–	25 000 000	500 000	9	30.2	1.5	0.1	–	80	30
YHR	1	5	–	15 000 000	1500 000	9	30.2	1.5	0.1	–	90	20
J	1	5	–	5000 000	500 000	6.5	37.9	1.5	0.1	–	134	30
JHR	1	5	–	15 000 000	1500 000	6.5	37.9	1.5	0.1	–	90	20
F	1	5	–	5000 000	500 000	4	51.7	1.5	0.1	–	134	30
G	0.5	5	–	5000 000	500 000	9	24.0	1.5	0.1	–	134	30
C	1	5	–	5000 000	500 000	9	30.2	–	–	0.45	134	30
YG	1	5	2.5	5000 000	500 000	9	30.2	1.5	0.1	–	134	30
EG	1	15	2.5	5000 000	1500 000	9	30.2	2.5	1.2	–	134	30
FG	1	5	2.5	5000 000	500 000	4	51.7	1.5	0.1	–	134	30

with conventional wisdom, is that, while thin discs very much like that of our Galaxy form in many simulations, if a thick disc is required at the current epoch, it has to be added to the ICs. So in Section 5 we explore non-standard disc masses and structures of the dark halo, and show that adopting a non-standard disc or halo, while not solving the problem of thick-disc formation, spoils the good agreement with observation found earlier as regards the bar and thin disc. In Section 6, we discuss the idealizations and potential missing ingredients of our models. Finally, in Section 7 we sum up and consider future work.

2 SIMULATIONS

We analyse a large set of controlled simulations of growing galactic discs embedded in non-growing dark matter haloes. These simulations were all carried out with the tree smoothed particle hydrodynamics (TreeSPH) code GADGET-3, last described in Springel (2005). We apply different gravitational softening lengths ϵ for baryonic and dark matter particles (listed as $\epsilon_{\rm DM}$ and $\epsilon_{\rm b}$ in Table 1) and use an opening angle $\theta = 0.5$ for the tree code. We use an adaptive time-stepping scheme in which time-steps are fractions $\Delta_j \equiv \tau/2^j$ of a base time-step $\tau < 10\,{\rm Myr}$ chosen by the code: the ith particle is assigned time-step Δ_j when

$$\Delta_j < \sqrt{\frac{2\eta\epsilon_i}{|\boldsymbol{a}_i|}} < \Delta_{j-1}, \tag{1}$$

where $\boldsymbol{a}_i$ and ϵ_i are the particle's gravitational acceleration and softening length, respectively, and $\eta = 0.02$ is an accuracy parameter. The hydrodynamical time-step is based on a Courant-like condition $\Delta_{i,\,\rm hyd} \propto \kappa h_i/c_{\rm s}$, where $\kappa = 0.15$ is the Courant parameter, h_i is the smoothing length and $c_{\rm s}$ is the sound speed. We apply an isothermal equation of state $P = \rho c_{\rm s}^2$ and use $N_{\rm SPH} = 48$ neighbours for the smoothing kernel. For further code details, we refer to Springel (2005).

2.1 Initial conditions

To generate ICs for our numerical experiments, we use the publicly available GALIC code (Yurin & Springel 2014), which produces near-equilibrium ICs of multi-component collisionless systems with given density distributions using an iterative approach.

The initial systems consist of a dark halo with a mass in the range of $M_{\rm DM} = (0.5\text{–}1) \times 10^{12}\,{\rm M}_\odot$ represented by $N_{\rm DM} = (1\text{–}25) \times 10^6$ particles and an embedded baryonic component. The ICs feature an initial baryonic component in the form of a disc or a bulge of mass $M_{\rm b,i} = (0.2\text{–}1.5) \times 10^{10}\,{\rm M}_\odot$ represented by $N_{\rm b,i} = (2\text{–}45) \times 10^5$ particles, so that the corresponding baryonic particle masses are in the range $m_{\rm b} = (3.3\text{–}25) \times 10^3\,{\rm M}_\odot$.

The density of the dark halo is given by (Hernquist 1990)

$$\rho_{\rm DM}(r) = \frac{M_{\rm DM}}{2\pi}\frac{a}{r\,(r+a)^3}. \tag{2}$$

The inner profile is adjusted so that it is similar to an NFW profile with concentration $c_{\rm halo} = 4\text{–}9$ and virial velocity $V_{200} \sim 130\text{–}170\,{\rm km\,s^{-1}}$. The scale radii are in the range $a = 24\text{–}52\,{\rm kpc}$. The halo initially has a spherical density profile and radially isotropic kinematics, i.e. equal velocity dispersion in the principal directions, $\sigma_r = \sigma_\phi = \sigma_\theta$ and consequently the anisotropy parameter $\beta = 1 - (\sigma_\theta^2 + \sigma_\phi^2)/(2\sigma_r^2) = 0$.

Our IC bulge components are set up with the same structure as those in Yurin & Springel (2014) and have a Hernquist density

profile with scalelength $a_{\rm bulge}$ which is distorted to be mildly oblate with axial ratio $s = 1.15$ as

$$\rho_{\rm bulge}(R, z) = s\,\rho_{\rm Hernquist}\left(\sqrt{R^2 + s^2 z^2}\right). \quad (3)$$

We choose $a_{\rm bulge} \sim 500$ pc, which is smaller than the 800 pc found by Widrow & Dubinski (2005) in their multi-component MW models with a Hernquist bulge, as we would like to test the impact of a compact bulge and as the MW bulge has likely grown over time due to secular processes. The bulge initially has no net rotation and the velocity structure is axisymmetric.

Disc components are set up with a mass profile

$$\rho_{\rm disc,i}(R, z) = \frac{M_{\rm b,i}}{4\pi z_{0,\rm disc} {h_{R,\rm disc}}^2}\,{\rm sech}^2\left(\frac{z}{z_{0,\rm disc}}\right)\exp\left(\frac{-R}{h_{R,\rm disc}}\right), \quad (4)$$

with an exponential scalelength $h_{R,\rm disc} = 1.5$–2.5 kpc and a radially constant isothermal vertical profile with scaleheights in the range $z_{0,\rm disc} = 0.1$–1.2 kpc. The vertical velocity dispersion σ_z thus declines with radius. For the ICs which start with a thin disc with $z_{0,\rm disc} \sim 0.1$ kpc, we assume $\sigma_z^2/\sigma_R^2 = 0.5$, so that Toomre's Q shows a minimum value of $Q_{\rm min} = 1.15$ for our standard halo. For hotter IC discs, we assume $\sigma_z^2/\sigma_R^2 = 1.0$.

For simulations with gas components, we include a thin gas disc in the ICs. For the YG and FG sets of ICs (see Table 1), the initial gas disc is created by turning a randomly chosen 5 per cent of stellar particles in a Y or F IC into SPH particles. We choose a low initial gas mass so that the disturbance of the IC is mild and unimportant compared to the rapid onset of disc instability in the growing galaxy. For the EG set of ICs, we turn 1.66 per cent of star particles in the E IC into gas particles, so that the initial gas mass is the same as in YG and FG. For EG gas particles, we choose only particles that lie close to the plane.

As far as in-plane kinematics of discs are concerned, we have modified the GALIC code in the following way: Yurin & Springel (2014) assume that the in-plane velocity dispersion is set by $\sigma_\phi^2 = \langle v_\phi^2\rangle - \langle v_\phi\rangle^2 = \sigma_R^2$, which contradicts the epicycle approximation, which for low σ_R yields $\sigma_\phi^2/\sigma_R^2 \simeq 0.5$. This approximation is, however, only expected to be valid for $\sigma_R \lesssim 10\,{\rm km\,s^{-1}}$ (e.g. fig. 4.16 in Binney & Tremaine 2008). Indeed, ICs of discs set with $\sigma_\phi = \sigma_R$ are unstable in the sense that σ_ϕ^2/σ_R^2 adjusts to a value which varies with σ_R, with a global mean value 0.66 for thin-disc ICs. We set up the ICs such that $\sigma_\phi^2/\sigma_R^2 = 0.66$ at all radii and apply a phase mixing procedure to allow an adjustment to the correct radial variation of σ_ϕ^2/σ_R^2. We take the output ICs of GALIC and integrate each particle's equations of motion in the fixed potential given by all particles at the output time until the radial component of velocity, v_r, has changed from negative to positive values at least eight times. We then select a random point in time during the integrated time-span and adopt the corresponding phase space coordinates as the new ICs. We find that we thus greatly suppress initial variations for σ_ϕ and σ_R. For an MW-like, stable disc with $Q_{\rm min} = 2$ and $N_{\rm disc} = 10^6$, we find that the dispersions at $R = 5h_R$ change by <10 per cent over 5 Gyr. The changes are still smaller at smaller radii.

2.1.1 *Selected ICs*

Table 1 provides an overview of all ICs. The first row describes the most important IC, that labelled Y. It comprises a halo of $10^{12}\,{\rm M}_\odot$ distributed over 5×10^6 particles with softening length 134 pc. The dark matter halo of the MW is generally expected to have a mass close to this value (Xue et al. 2008). The halo's scalelength implies a concentration $c = 9$ close to that predicted for the MW by cosmology (Zhao et al. 2009). Moreover, similar halo parameters were adopted for the model of Aumer & Schönrich (2015), which fulfilled constraints on Snhd circular velocity and dark matter mass within the solar radius. The stellar disc of our standard IC Y is compact and thin and contains only a small mass fraction (10 per cent for most models) of the final disc mass of the models. It has scalelength $h_{R,\rm disc} = 1.5$ kpc and scaleheight $z_{0,\rm disc} = 0.1$ kpc, and it contains $5 \times 10^9\,{\rm M}_\odot$ distributed over 5×10^5 particles with softening length 30 pc. The Y IC includes no gas and no bulge.

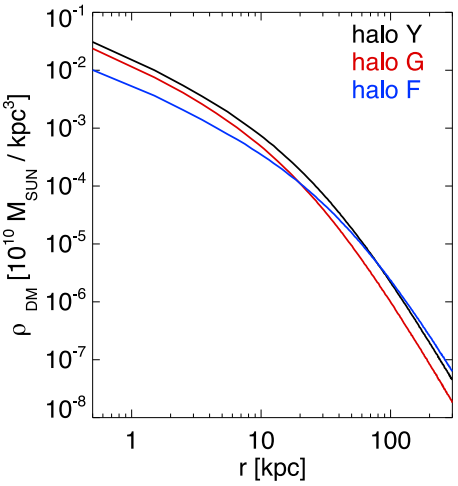

Figure 1. The radial density profiles of the standard dark halo (Y) and of two non-standard dark haloes: that of F has a lower concentration, while that of G has half the mass.

The purpose of the next three ICs listed in Table 1, Z, A and E, is to test the impact of thicker initial discs. They have discs that are twice and three times more massive than in the Y IC, with correspondingly increased numbers of star particles. These more massive discs are associated with greatly increased scaleheights, and in the case of E an increased scalelength. IC EHR is a higher resolution version of IC E.

IC S below these in Table 1 differs from Y in having a mere $2 \times 10^9\,{\rm M}_\odot$ in its disc.

In the next series of ICs in Table 1, we vary the numbers of particles in halo and/or disc. They are all based on IC Y. YLR is a lower resolution version of Y, while YHR is a higher resolution version. For YLH we reduce $N_{\rm DM}$, but keep $N_{\rm b,i}$ the same and in YHH we increase $N_{\rm DM}$ for constant $N_{\rm b,i}$.

To create models with lower central dark matter densities, the next group of ICs, J, F and G, differ from Y in the scalelengths $a_{\rm halo}$ of their dark haloes. F has the standard halo mass but $a_{\rm halo}$ increased to 51.7 from 30.2 kpc, while G has only half the standard mass in its halo but a small scalelength, $a_{\rm halo} = 24$ kpc. As Fig. 1 demonstrates, increasing $a_{\rm halo}$ at fixed mass lowers the density of dark matter in the central $\sim$10 kpc, which is the relevant region for our experiments, where the vast majority of stars live. The halo of IC J is intermediate to those of ICs Y and F, while IC JHR is a higher resolution version of J.

IC C differs from Y in having a bulge rather than a disc.

The final group of ICs in Table 1, YG, EG, FG, are the only ICs to include gas, $2.5 \times 10^8\,{\rm M}_\odot$ of it. As their names suggest, YG results from adding the gas to Y, EG results from adding gas to E and FG is obtained by adding gas to F.

2.2 Feeding the disc

2.2.1 Adding stars

To model the continuous growth of galactic discs via SF, we add new disc particles with masses $m_{\rm b}$ as determined by the baryonic particle masses in the ICs to the existing disc every 5 Myr. For most models, we assume a star formation rate (SFR) given by

$$\mathrm{SFR}(t) = \mathrm{SFR}_0 \times \exp\left(-\frac{t}{t_{\rm SFR}}\right), \tag{5}$$

which we refer to as *type 1* SFR. The models use an exponential decay time-scale $t_{\rm SFR} = 4$–16 Gyr, which is motivated by the findings of Aumer & Binney (2009). The specific choice of $t_{\rm SFR}$ in this range has a minor influence on the results presented here, which is why we focus on models with $t_{\rm SFR} = 8$ Gyr. The normalization SFR_0 is always adjusted to yield a total inserted baryonic mass, including the disc mass from the ICs, of $M_{\rm f} \sim (3$–$8) \times 10^{10}\,\mathrm{M}_\odot$ after a time $t_{\rm f} = 10$ Gyr [Piffl et al. (2014) find $M_{\rm MW} = (5.6 \pm 1.6) \times 10^{10}\,\mathrm{M}_\odot$ for the MW].

For two models, we add an initial phase of increasing SFR through

$$\mathrm{SFR}(t) = \mathrm{SFR}_0 \times \exp\left(-\frac{t}{t_{\rm SFR}} - \frac{0.5\ \mathrm{Gyr}}{t}\right). \tag{6}$$

We refer to this SFR law as *type 2* SFR. These models are evolved for $t_{\rm f} = 12$ Gyr and the normalization SFR_0 is adjusted accordingly. When modelling the chemical evolution of the disc, inclusion of the period in which the SFR increases proves vital (Sanders & Binney 2015). Since we do not consider chemistry, the differences between models run with type 1 and type 2 SFR prove to be modest.

Note that due to the nature of our simulations, the final number of particles in the disc $N_{\rm b,f} = M_{\rm f}/m_{\rm b} \gg N_{\rm b,i}$. For most simulations $N_{\rm b,f} \approx N_{\rm DM}$.

The added disc mass is radially distributed as $\Sigma(R) \propto \exp\left(-R/h_R(t)\right)$, with an exponential scalelength that varies with time as

$$h_R(t) = h_{R,\rm i} + \left(h_{R,\rm f} - h_{R,\rm i}\right)(t/t_{\rm f})^{\xi}. \tag{7}$$

Note that at $h_R(0)$ is not necessarily equal to the scalelength $h_{R,\rm disc}$ of the IC. An increase in scalelength from $h_{R,\rm i}$ to $h_{R,\rm f}$ at $t_{\rm f}$ for the pattern of accretion simulates inside-out growth of discs, which is suggested by observations of MW stellar populations (Bensby et al. 2011; Bovy et al. 2012a) and external galaxies (Wang et al. 2011a) and also by cosmological models of disc galaxy formation (Aumer, White & Naab 2014). Bovy et al. (2012a) find scalelengths in the range $h_R \sim 1.5$–5 kpc for their MW mono-abundance populations, and we test different radial growth histories within this range. The particles start from $z = 0$ and randomly chosen values of the azimuth ϕ. The coordinate system is regularly updated to be centred on the centre of mass of the system.

The particles are assigned near-circular orbits. We determine the new particles' rotational velocities as $v_\phi = \sqrt{a_R(R)R}$, where $a_R(R)$ is the azimuthal average of the radial gravitational acceleration, $\partial\Phi/\partial R$. To this value of v_ϕ, we add random velocity components in all three directions ϕ, R and z, drawn from Gaussian distributions of dispersion σ_0. For most models, $\sigma_0 = 6\,\mathrm{km\,s^{-1}}$ is small and constant, in agreement with young local stars (Aumer & Binney 2009). We have run one model with $\sigma_0 = 10\,\mathrm{km\,s^{-1}}$ and found that it does not change our results in any significant way. Motivated by observations of turbulent discs at high redshift (e.g. Wisnioski et al. 2015), for some models we assume that $\sigma_0(t)$ declines from a large initial value as

$$\sigma_0(t) = \left[6 + 30\exp(-t/1.5\ \mathrm{Gyr})\right]\ \mathrm{km\,s^{-1}}. \tag{8}$$

Note that as we place all particles at $z = 0$, the measured vertical dispersion of an unheated component after insertion is smaller than σ_0, as the mid-plane is at the bottom of the vertical potential well and particles lose kinetic energy moving away from it.

After a disc has developed a bar, there are no longer circular orbits in the bar region. We can avoid this problem by introducing an inner cutoff radius $R_{\rm cut}$, within which no particles are introduced. Our standard approach is to set $R_{\rm cut}$ to the smaller of 5 kpc and the radius at which the Fourier amplitude of the stellar component

$$A_2(R) \equiv \frac{1}{N(R)}\sum_{j=1}^{N(R)} \mathrm{e}^{2\mathrm{i}\phi_j} \tag{9}$$

drops below $\mathrm{e}^{-1.5}$. Here $N(R)$ is the number of particles in a thin cylindrical shell centred on R and ϕ_j is the azimuth of particle j. The majority of models are unaffected by the upper limit on $R_{\rm cut}$ as few bars reach 5 kpc.

There are models for which our standard 'adaptive' cutoff brings along problems, which leads us to also use different approaches. In the presence of an early strong bar, the adaptive cutoff very soon rises to its limiting value, 5 kpc. After a fraction of a gigayear, $R_{\rm cut}$ decreases again. To avoid this early ring-like phase of growth, we have run additional models with $R_{\rm cut}$ limited to 1 kpc during the first Gyr and 3 kpc during the first 3 Gyr. We refer to this as an 'AdapLi cutoff'.

Unfortunately, adaptive cutoffs make radial SFHs model dependent. For some of our experiments, such as resolution tests or comparisons of heating efficiencies, this effect makes the results harder to interpret. Therefore, we use a 'fixed' cutoff for certain subsets of our models. If these models have type 1 SFR, we fix the evolution of the cutoff radius to

$$R_{\rm cut}(t) = \left(0.67 + \frac{0.33t}{1\ \mathrm{Gyr}}\right)\ \mathrm{kpc} \tag{10}$$

at times $t > 1$ Gyr. This rule mimics bar growth histories in test simulations with $R_{\rm cut} = 0$ and no GMC particles.

For model Y5fs4m2 (see Table 3 and Section 2.4 for details on the models and their names) which features a type 2 SFR, the cutoff is only introduced after 3 Gyr and then grows in the same way starting at 1 kpc. This reduces the impact of particles on initially inappropriate orbits and also reduces the computational cost as particles at greater radii on average have larger time-steps. Additionally, it is not clear how the radial growth of galaxies happens in detail. Cosmological simulations of forming disc galaxies by Aumer et al. (2014) find that growing discs can display an inner region depleted of gas and SF.

In addition to models with different cutoffs, we have also run a small number of test models, in which no cutoff was applied. As already mentioned, the choice of cutoff can influence the results of the models. When this is the case for the analysis of this paper, it is pointed out in the text. In other cases, the conclusions are not affected by this choice.

2.2.2 Adding and removing smooth gas

The significance for galactic dynamics of the smoother component of the interstellar medium that is the topic of this section is that, as a dissipative medium, it responds to the non-axisymmetric part of the

gravitational field in a different way to stars. Our goal is to capture this essential difference with the simplest possible model. We model gas with an isothermal equation of state $P = \rho c_s^2$, where $c_s = 10$ or $20\,\mathrm{km\,s^{-1}}$ is the sound speed [Sormani, Binney & Magorrian (2015) find that the effective sound speed in the ISM is $c_s \gtrsim 10\,\mathrm{km\,s^{-1}}$]. We grow the disc by continuously adding star and gas particles. We achieve a roughly constant global fraction f_g of the disc mass that comprises gas as follows: if the ratio of gas mass to total mass in the disc exceeds f_g, a fraction f_g of the particles added to the disc in that time-step are gas particles; if the gas-to-total mass ratio is less than f_g, a fraction $2f_g$ of the added particles are gas particles. As our gas ICs have lower gas fractions than the values of f_g we use, gas simulations start with a period during which $2f_g$ of the added particles are gas particles.

To keep our models simple, we choose a constant gas fraction. Typical local star-forming disc galaxies have gas fractions $f_g = 0.05$–0.25 (Young & Scoville 1991), whereas we test $f_g = 0.1$–0.3. Gas fractions have been shown to be higher at redshifts $z \sim 2$ (e.g. Tacconi et al. 2010). However, we here only model the smooth interstellar gas. Our model for molecular clouds is described in Section 2.3 and produces, for typical parameters, a GMC fraction, which declines from $f_{\rm GMC} > 0.3$ at early times to $f_{\rm GMC} < 0.05$ at late times. We find that parameters f_g and c_s in the ranges chosen for our models have a minor effect on our results.

High gas densities in the centres of model galaxies are computationally expensive, so we limit the central gas density as follows. (i) We do not add gas particles at $R < 1$ kpc. Otherwise the same inner cutoff $R_{\rm cut}$ as for star particles is applied. (ii) We model SF in the central galaxy by identifying gas particles with hydrogen number densities $n > n_{\rm th} = 10\,\mathrm{cm^{-3}}$ and specific angular momentum $j_z < j_{\rm th} = 100\,\mathrm{kpc\,km\,s^{-1}}$. Such particles become the sites of SF with a probability $p = 1 - \exp(-\nu\Delta t_i/t_{\rm dyn})$, where $\nu = 0.1$ is an efficiency parameter, $t_{\rm dyn} = 1/\sqrt{4\pi G\rho}$ is the local dynamical time-scale and Δt_i is the time-step of the particle (e.g. Lia, Portinari & Carraro 2002). For each particle which is turned into a star, four gas particles which fulfil the SF criteria are removed from the simulation. This rule is designed to mimic the effect of a central galactic outflow (Shopbell & Bland-Hawthorn 1998; Bland-Hawthorn & Cohen 2003). In practice, the above SF algorithm comes into action only in the innermost $\sim$2 kpc, where gas densities are high and material has low angular momentum. The region within which it is active grows with increasing f_g, decreasing c_s and decreasing h_R.

As stated above, when the fraction of the disc mass that comprises gas falls below f_g, a fraction $2f_g$ of added particles comprise gas. If the rate of consumption of gas by SF in the central region is modest, adding a fraction $2f_g$ of gas particles causes the fraction of the disc mass that comprises gas to rise until it reaches f_g, when the fraction of added particles that comprise gas drops to f_g. Hence, so long as the rate of consumption of gas at the centre is modest, the gas fraction oscillates around f_g. But for a sufficiently large rate of central SF, even adding a fraction $2f_g$ of gas particles does not avert decline of the gas fraction. Hence, it can happen that the gas fraction in the disc falls below f_g, but it cannot rise significantly above this value.

$M_{\rm f}$ (final baryonic mass) is defined to be the sum of the masses of IC particles and all added particles, whether stars or gas. On account of the ejection of gas by central SF, in models with gas the baryonic mass of the final disc is always less than $M_{\rm f}$.

2.3 Simulating GMCs

Although GMCs are composed of gas, in our models, we treat them separately from the less dense gas that occupies much of the Galactic plane. To model the impact of a population of GMCs on the dynamics of the disc, we introduce a population of very massive particles. As stars form in GMCs, the total mass of GMCs present is determined by the SFR and the efficiency of SF ζ, which gives the fraction of mass of a GMC that turns into stars before supernovae completely destroy the GMC. For the MW, Murray (2011) finds $\zeta = 0.08$. GMCs are short-lived, with lifetime $\tau_{\rm GMC} < 100$ Myr: Murray (2011) finds $\tau_{\rm GMC} \sim 27$ Myr for massive GMCs in the MW and Meidt et al. (2015) find a very similar value, $\tau_{\rm GMC} \sim 20$–30 Myr, for inter-arm clouds in M51. However, Murray (2011) also remarks that to account for the total molecular mass in the MW one has to assume that molecular gas spends no more than half its time in clouds, and the rest assembling and dispersing.

We translate these facts into our models by adding a mass $\Delta m_{\rm GMC} = \Delta m_{\rm stars}/\zeta$ in GMCs whenever we add a mass $\Delta m_{\rm stars}$ in stars. A GMC lives for $\Delta t_{\rm GMC} = 50$ Myr. The mass of a GMC particle is a function of time:

$$m(t) = m_{\rm i} \times \begin{cases} \zeta + t_{25}^2\,(1-\zeta) & t_{25} < 1, \\ 1 & 1 < t_{25} < 2, \end{cases} \tag{11}$$

where $t_{25} \equiv t/25$ Myr. Hence, in the first half of its 50 Myr life, a cloud assembles from an initial mass $\zeta m_{\rm i}$, and then its mass is constant at $m_{\rm i}$ until a burst of supernovae suddenly destroys it. $\Delta m_{\rm GMC}$ is the total mass a coeval population of GMCs has reached after 25 Myr.

The typical sizes of massive GMCs in the MW are $l_{\rm GMC} \sim 10$–100 pc (e.g. Murray 2011), close to the gravitational softening length $\epsilon_{\rm disc} = 30$ pc of our disc particles in our standard resolution. We therefore also model the GMC particles with $\epsilon_{\rm GMC} = 30$ pc, which is advantageous because when particles with differing softening lengths interact, the code uses the longer length. When increasing (decreasing) our resolution, we decrease (increase) the softening lengths for dark matter particles, but keep $\epsilon_{\rm GMC}$ the same. $\epsilon_{\rm disc}$ is only changed for increased resolution, when it is decreased.

GMC particles are introduced on near-circular orbits as described above for star particles, assuming random velocity components with $\sigma_0 = 6\,\mathrm{km\,s^{-1}}$. We have tested setting $\sigma_0 = 0$ for GMCs and found no significant changes to the results. Their radial distribution is the same as that of the stars added at the same time except that we impose an outer cutoff at $R = R_{\rm cut} + 6h_R$. The cutoff prevents heavy GMC particles arising in the disc outskirts, where in real galaxies no dense gas clouds are found.

In real galaxies, GMCs are preferentially found in higher density disc structures such as spiral arms and/or rings. To determine how the specific spatial distribution of GMCs influences the heating process, we do not distribute them uniformly in azimuth, as we do for star and gas particles. Instead, we make the density of added GMCs be

$$\rho_{\rm GMC}(R,\phi) \propto \rho_{\rm ys}^{\alpha}(R,\phi), \tag{12}$$

where $\rho_{\rm ys}(R,\phi)$ is the density of young star particles with ages between 200 and 400 Myr, and α is a parameter. The youngest stars are not included because they are introduced randomly in azimuth and need time to fall in with structure in the disc, and older stars are excluded as they are hotter and display weaker azimuthal structure. If $\alpha = 0$, GMC particles are added uniformly in azimuth, whereas if $\alpha > 0$, any structure displayed by young stars is reinforced by added GMCs. We determine $\rho_{\rm ys}(R,\phi)$ by binning stars into 120 azimuthal and 36 radial bins, with the radial extent of bins increasing with R.

Real GMCs have a spectrum of masses. Mass functions are usually described as power laws

$$\frac{\mathrm{d}N}{\mathrm{d}M} \propto M^{\gamma} \text{ for } M < M_{\rm up}. \quad (13)$$

Details of mass functions, such as γ and the upper cutoff mass $M_{\rm up}$, vary between galaxies and even within a galaxy (e.g. Rosolowsky 2005; Colombo et al. 2014). In Local Group galaxies, γ varies between -1.4 and -2.9 (Rosolowsky 2005), and thus between top-heavy and bottom-heavy distributions. The most massive GMCs in the inner MW have $M \sim 3 \times 10^6\,\mathrm{M}_\odot$, which is the number often used for $M_{\rm up}$ (Rosolowsky 2005), but objects with masses close to $M \sim 10^7\,\mathrm{M}_\odot$ are also known (Murray 2011; García et al. 2014), although they are usually considered to be cloud complexes. For M51, the mass distributions have been measured to extend to $M_{\rm up} \sim 10^7\,\mathrm{M}_\odot$ (Colombo et al. 2014).

To account for these uncertainties, we ran models with a range of values for γ and $M_{\rm up}$. In most of our models, we assume that all mass in GMCs sits in distributions with a lower mass limit of $M_{\rm low} = 10^5\,\mathrm{M}_\odot$. If the assumed mass function is not a delta function, we sample it with eight different masses of GMC particles. For mass functions with $M_{\rm up} = 1 \times 10^7\,\mathrm{M}_\odot$, the particle masses are $\{0.25, 0.5, 1, 2, 4, 6, 8, 10\} \times 10^6\,\mathrm{M}_\odot$ and for $M_{\rm up} = 3 \times 10^6\,\mathrm{M}_\odot$ they are $\{0.1, 0.2, 0.4, 0.6, 0.8, 1, 2, 3\} \times 10^6\,\mathrm{M}_\odot$. We do not include a radial variation of GMC mass function, such as is observed in the MW (Rosolowsky 2005).

2.4 Models run

Tables 2 and 3 (which together form a single long table) list 94 gas-free models we have run for at least 10 Gyr plus model YHHN1f, which only ran until 9.3 Gyr due to a shortage of resources. We here describe these models and their naming convention. Our 10 models that include an isothermal gas component are listed in Table 4. Models that contribute to one of our figures are marked with boldface names.

These are all the models we currently have available. As the number is limited by computational resources, and our rather large number of parameters prevented us from a rigorous sampling of parameter space, we employed a two-fold strategy. (i) We intended to understand how variations of parameters affect the results. (ii) We intended to understand the phenomena displayed by all or a subset of the simulations. For (ii) we thus explored some regions of parameter space more densely than others.

Model names all start with one to three capital letters identifying their IC as listed in Table 1. Standard models have GMCs, but no gas. If there are no GMCs present, we add 'N' to the name. The presence of isothermal gas can be inferred from the added 'G' in the IC name.

These capital letters are followed by a number running from 1 to 7 describing the radial growth history of the model, determined by parameters $h_{R,\rm i}$, $h_{R,\rm f}$ and ξ. The most common growth histories are '1', which stands for inside-out growth starting from the IC $h_{R,\rm i} = h_{R,\rm disc}$ and increasing as $t^{\xi=0.5}$ to $h_{R,\rm f} = 4.3$ kpc, and '2', which stands for a constant scalelength of $h_{R,\rm i} = h_{R,\rm f} = 2.5$ kpc.

Each model name contains at least one capital letter for the IC and a number for the growth history. For all other parameters, we define standard values. Only if a model deviates in one or more parameters from the standard, additional digits are added to the model name as follows.

(i) Standard models use an adaptive inner cutoff $R_{\rm cut}(t)$. If we use a fixed cutoff as described by equation (10), we add 'f' to the name, if we use no cutoff we add 'n' and for an AdapLi cutoff we add 'l'.

(ii) The vast majority of our models assume final baryonic mass $M_{\rm f} = 5 \times 10^{10}\,\mathrm{M}_\odot$. We have two models each with $M_{\rm f} = 3 \times 10^{10}\,\mathrm{M}_\odot$ (labelled 'Mb−') and $M_{\rm f} = 7.5 \times 10^{10}\,\mathrm{M}_\odot$ (labelled 'Mb+').

(iii) The overall SFH of a model is described by the SFR type, the final time $t_{\rm f}$ and the SF time-scale $t_{\rm SFR}$. Our standard choice is a type 1 SFR with $t_{\rm f} = 10$ Gyr and $t_{\rm SFR} = 8$ Gyr. We have explored four additional SFHs, which are labelled by 's2',...,'s5'.

(iv) The standard input velocity dispersion $\sigma_0 = 6\,\mathrm{km\,s^{-1}}$. We have one model with $\sigma_0 = 10\,\mathrm{km\,s^{-1}}$ (labelled 'σ') and several with $\sigma_0(t) = (6 + 30\mathrm{e}^{-t/1.5\,\mathrm{Gyr}})\,\mathrm{km\,s^{-1}}$ (labelled 'τ').

(v) The GMC SF efficiency ζ has a standard value of 0.08. A lower $\zeta = 0.04$ is labelled as '$\zeta-$', and a higher value of $\zeta = 0.16$ is labelled as '$\zeta+$'.

(vi) $\alpha = 1.0$ is the standard choice for the parameter controlling the azimuthal density profile of GMCs. We have tested three differing values: $\alpha = 0.0$ is labelled 'α0', $\alpha = 1.5$ is labelled 'α1' and $\alpha = 2.0$ is labelled 'α2'.

(vii) The standard parameters controlling the GMC mass function are $M_{\rm low} = 10^5\,\mathrm{M}_\odot$, $M_{\rm up} = 10^7\,\mathrm{M}_\odot$ and $\gamma = -1.6$. We have tested five additional mass functions, which we label 'm2',...,'m6'.

(viii) For the gas parameters, our standards are $c_{\rm s} = 10\,\mathrm{km\,s^{-1}}$ and $f_{\rm g} = 0.1$. $c_{\rm s} = 20\,\mathrm{km\,s^{-1}}$ is labelled as 'c2', and higher values of $f_{\rm g}$ are labelled as 'g2' and 'g3'.

3 ROBUSTNESS OF RESULTS

Our simulations have value only if satisfactory answers can be given to two questions: (i) how sensitive are the final models to details of the ICs from which they are derived? and (ii) would the final models change significantly if more particles were used to represent the galaxy? We now address these questions. Unless mentioned otherwise, all results in this paper are presented at final time $t = t_{\rm f}$ of the simulation and for results at $R = 8$ kpc we consider an annulus which is 1 kpc wide and centred on $R = 8$ kpc.

3.1 Impact of the initial baryonic mass

Does the rather arbitrary mass $M_{\rm b,\,i}$ of our IC discs have a significant impact on a model's evolution? Fig. 2 addresses this question by showing radial surface density profiles and vertical density profiles at $R = 8$ kpc for two models, Y1f and S1f, that differ only in that S1f's IC disc has only 40 per cent of the mass of Y1f's IC disc. At fixed baryonic mass $M_{\rm f}$, a reduction in the mass $M_{\rm b,i}$ of the IC has to be compensated by adding more mass later, using a longer scalelength on average. Consequently, decreasing $M_{\rm b,i}$ makes the model less centrally concentrated, which weakens the central bar, if any. In the lower panel of Fig. 2, the reduction in bar mass causes the red curve of S1f to underlie the black one of Y1f at $R \lesssim 2$ kpc. We shall see below that a weaker bar also accounts for the red curve underlying the black one in the upper panel at $|z| \gtrsim 1$ kpc. However, from Fig. 2 it is clear that a 60 per cent reduction in the mass of the initial disc changes the final model very little. Hence, our models are insensitive to $M_{\rm b,i}$. Comparison of models Y2/S2 and YN1/SN1 yields the same conclusion. As $M_{\rm b,i}$ is supposed to be small compared to $M_{\rm f}$, testing higher values of $M_{\rm b,i}$ in thin-disc ICs would be pointless. Models with $M_{\rm b,i} = 0$ would be problematic because an initial disc defines a disc plane,

Table 2. List of gas-free models; Models that contribute to a figure have bold names. Column 1: model name; column 2: initial conditions; column 3: GMCs Yes/No; column 4: cutoff: No, Adaptive (no new particles in bar region), fixed (pre-defined evolving inner cutoff for new particles) or AdapLi (see the text); column 5: final time t_f; column 6: total inserted baryonic model mass M_f (including initial baryonic mass); column 7: initial disc scalelength $h_{R,i}$; column 8: final disc scalelength $h_{R,f}$; column 9: scalelength growth parameter ξ; column 10: type of SFR law; column 11: exponential decay time-scale t_{SFR} for the star formation rate; column 12: initial velocity dispersion for inserted stellar particles, σ_0; column 13: GMC star formation efficiency ζ; column 14: GMC azimuthal density distribution parameter α; column 15: GMC mass function lower and upper mass cutoffs M_{low}, M_{up}; column 16: GMC mass function power-law index.

(1) Name	(2) ICs	(3) GMCs	(4) Cutoff	(5) t_f (Gyr)	(6) $M_f/M_\odot$ (10^{10})	(7) $h_{R,i}$ (kpc)	(8) $h_{R,f}$ (kpc)	(9) ξ	(10) SFR type	(11) t_{SFR} (Gyr)	(12) σ_0 (km s^{-1})	(13) ζ	(14) α	(15) $M_{low\text{-}up}$ (10^5 $M_\odot$)	(16) γ
Y1	Y	Yes	Adap	10	5	1.5	4.3	0.5	1	8.0	6	0.08	1.0	1–100	−1.6
Y1f	Y	Yes	Fix	10	5	1.5	4.3	0.5	1	8.0	6	0.08	1.0	1–100	−1.6
Y1n	Y	Yes	No	10	5	1.5	4.3	0.5	1	8.0	6	0.08	1.0	1–100	−1.6
Y2	Y	Yes	Adap	10	5	2.5	2.5	0.0	1	8.0	6	0.08	1.0	1–100	−1.6
Y3	Y	Yes	Adap	10	5	1.5	3.0	0.5	1	8.0	6	0.08	1.0	1–100	−1.6
Y3f	Y	Yes	Fix	10	5	1.5	3.0	0.5	1	8.0	6	0.08	1.0	1–100	−1.6
Y4	Y	Yes	Adap	10	5	1.5	2.2	0.5	1	8.0	6	0.08	1.0	1–100	−1.6
Y4f	Y	Yes	Fix	10	5	1.5	2.2	0.5	1	8.0	6	0.08	1.0	1–100	−1.6
Y5	Y	Yes	Adap	10	5	1.5	3.5	0.5	1	8.0	6	0.08	1.0	1–100	−1.6
Y6	Y	Yes	Adap	10	5	1.5	3.0	0.2	1	8.0	6	0.08	1.0	1–100	−1.6
Y7	Y	Yes	Adap	10	5	2.5	6.0	0.5	1	8.0	6	0.08	1.0	1–100	−1.6
Y1Mb−	Y	Yes	Adap	10	3	1.5	4.3	0.5	1	8.0	6	0.08	1.0	1–100	−1.6
Y1Mb+	Y	Yes	Adap	10	7.5	1.5	4.3	0.5	1	8.0	6	0.08	1.0	1–100	−1.6
Y2Mb−	Y	Yes	Adap	10	3	2.5	2.5	0.0	1	8.0	6	0.08	1.0	1–100	−1.6
Y2Mb+	Y	Yes	Adap	10	7.5	2.5	2.5	0.0	1	8.0	6	0.08	1.0	1–100	−1.6
Y1s2	Y	Yes	Adap	10	5	1.5	4.3	0.5	1	16.0	6	0.08	1.0	1–100	−1.6
Y1fs2	Y	Yes	Fix	10	5	1.5	4.3	0.5	1	16.0	6	0.08	1.0	1–100	−1.6
Y1fs3	Y	Yes	Fix	10	5	1.5	4.3	0.5	1	4.0	6	0.08	1.0	1–100	−1.6
Y4fs3	Y	Yes	Fix	10	5	1.5	2.2	0.5	1	4.0	6	0.08	1.0	1–100	−1.6
Y5s4	Y	Yes	Adap	12	5	1.5	3.5	0.5	2	8.0	6	0.08	1.0	1–100	−1.6
Y5fs4m2	Y	Yes	Fix	12	5	1.5	3.5	0.5	2	8.0	6	0.08	1.0	1–30	−1.6
Y5s5	Y	Yes	Adap	12	5	1.5	3.5	0.5	1	8.0	6	0.08	1.0	1–100	−1.6
Y1fσ	Y	Yes	Fix	10	5	1.5	4.3	0.5	1	8.0	10	0.08	1.0	1–100	−1.6
Y1fα2	Y	Yes	Fix	10	5	1.5	4.3	0.5	1	8.0	6	0.08	2.0	1–100	−1.6
Y1fα0	Y	Yes	Fix	10	5	1.5	4.3	0.5	1	8.0	6	0.08	0.0	1–100	−1.6
Y1fα1	Y	Yes	Fix	10	5	1.5	4.3	0.5	1	8.0	6	0.08	1.5	1–100	−1.6
Y1$\zeta-$	Y	Yes	Adap	10	5	1.5	4.3	0.5	1	8.0	6	0.04	1.0	1–100	−1.6
Y1l$\zeta-$	Y	Yes	AdapLi	10	5	1.5	4.3	0.5	1	8.0	6	0.04	1.0	1–100	−1.6
Y1f$\zeta-$	Y	Yes	Fix	10	5	1.5	4.3	0.5	1	8.0	6	0.04	1.0	1–100	−1.6
Y1f$\zeta+$	Y	Yes	Fix	10	5	1.5	4.3	0.5	1	8.0	6	0.16	1.0	1–100	−1.6
Y1fζ+m2	Y	Yes	Fix	10	5	1.5	4.3	0.5	1	8.0	6	0.16	1.0	1–30	−1.6
Y4$\zeta-$	Y	Yes	Adap	10	5	1.5	2.2	0.5	1	8.0	6	0.04	1.0	1–100	−1.6
Y4f$\zeta-$	Y	Yes	Fix	10	5	1.5	2.2	0.5	1	8.0	6	0.04	1.0	1–100	−1.6
Y1m2	Y	Yes	Adap	10	5	1.5	4.3	0.5	1	8.0	6	0.08	1.0	1–30	−1.6
Y1fm2	Y	Yes	Fix	10	5	1.5	4.3	0.5	1	8.0	6	0.08	1.0	1–30	−1.6
Y1nm2	Y	Yes	No	10	5	1.5	4.3	0.5	1	8.0	6	0.08	1.0	1–30	−1.6
Y1fm3	Y	Yes	Fix	10	5	1.5	4.3	0.5	1	8.0	6	0.08	1.0	10–10	δ fct.
Y1fm4	Y	Yes	Fix	10	5	1.5	4.3	0.5	1	8.0	6	0.08	1.0	1–100	−2.52
Y1fm5	Y	Yes	Fix	10	5	1.5	4.3	0.5	1	8.0	6	0.08	1.0	1–30	−1.78
Y1fm6	Y	Yes	Fix	10	5	1.5	4.3	0.5	1	8.0	6	0.08	1.0	1–100	−2.2
YN1	Y	No	Adap	10	5	1.5	4.3	0.5	1	8.0	6	–	–	–	–
YN1f	Y	No	Fix	10	5	1.5	4.3	0.5	1	8.0	6	–	–	–	–
YN2	Y	No	Adap	10	5	2.5	2.5	0.0	1	8.0	6	–	–	–	–
YN3	Y	No	Adap	10	5	1.5	3.0	0.5	1	8.0	6	–	–	–	–
YN3s2	Y	No	Adap	10	5	1.5	3.0	0.5	1	16.0	6	–	–	–	–
YN5s4	Y	No	Adap	12	5	1.5	3.5	0.5	2	8.0	6	–	–	–	–
YN7	Y	No	Adap	10	5	2.5	6.0	0.5	1	8.0	6	–	–	–	–

which is needed for insertion of particles with (almost) parallel angular-momentum vectors.

A major finding of this study is that in our models a thick disc like that of the MW must be present in the ICs, because it fails to form alongside the thin disc (Section 5.1). The insensitivity of the ICs implies that major changes in the ICs are required for the creation of a realistic thick disc. Specifically, even a three-fold increase in $M_{b,i}$ and a 10-fold increase in $z_{0,disc}$ over the values used in IC Y prove not quite sufficient to form a satisfactory thick disc.

Table 3. Continuation of Table 2.

(1) Name	(2) ICs	(3) GMCs	(4) Cutoff	(5) t_f (Gyr)	(6) $M_f/M_\odot$ (10^{10})	(7) $h_{R,i}$ (kpc)	(8) $h_{R,f}$ (kpc)	(9) ξ	(10) SFR type	(11) t_{SFR} (Gyr)	(12) σ_0 (km s^{-1})	(13) ζ	(14) α	(15) $M_{low\text{-}up}$ (10^5 M$_\odot$)	(16) γ
YLR1	YLR	Yes	Adap	10	5	1.5	4.3	0.5	1	8.0	6	0.08	1.0	1–100	−1.6
YHR1	YHR	Yes	Adap	10	5	1.5	4.3	0.5	1	8.0	6	0.08	1.0	1–100	−1.6
YHR2	YHR	Yes	Adap	10	5	2.5	2.5	0.0	1	8.0	6	0.08	1.0	1–100	−1.6
YLHN1f	YLH	No	Fix	10	5	1.5	4.3	0.5	1	8.0	6	–	–	–	–
YHHN1f	YHH	No	Fix	10	5	1.5	4.3	0.5	1	8.0	6	–	–	–	–
YHRN1f	YHR	No	Fix	10	5	1.5	4.3	0.5	1	8.0	6	–	–	–	–
Z1	Z	Yes	Adap	10	5	1.5	4.3	0.5	1	8.0	6	0.08	1.0	1–100	−1.6
Z1τ	Z	Yes	Adap	10	5	1.5	4.3	0.5	1	8.0	$6+30e^{-t_{1.5}}$	0.08	1.0	1–100	−1.6
Z2	Z	Yes	Adap	10	5	2.5	2.5	0.0	1	8.0	6	0.08	1.0	1–100	−1.6
ZN1	Z	No	Adap	10	5	1.5	4.3	0.5	1	8.0	6	–	–		–
ZN1τ	Z	No	Adap	10	5	1.5	4.3	0.5	1	8.0	$6+30e^{-t_{1.5}}$	–	–		–
A1	A	Yes	Adap	10	5	1.5	4.3	0.5	1	8.0	6	0.08	1.0	1–100	−1.6
A1τ	A	Yes	Adap	10	5	1.5	4.3	0.5	1	8.0	$6+30e^{-t_{1.5}}$	0.08	1.0	1–100	−1.6
A2	A	Yes	Adap	10	5	2.5	2.5	0.0	1	8.0	6	0.08	1.0	1–100	−1.6
A2τ	A	Yes	Adap	10	5	2.5	2.5	0.0	1	8.0	$6+30e^{-t_{1.5}}$	0.08	1.0	1–100	−1.6
AN1	A	No	Adap	10	5	1.5	4.3	0.5	1	8.0	6	–	–		–
AN1τ	A	No	Adap	10	5	1.5	4.3	0.5	1	8.0	$6+30e^{-t_{1.5}}$	–	–		–
E1	E	Yes	Adap	10	5	2.5	4.3	0.5	1	8.0	6	0.08	1.0	1–100	−1.6
E1τ	E	Yes	Adap	10	5	2.5	4.3	0.5	1	8.0	$6+30e^{-t_{1.5}}$	0.08	1.0	1–100	−1.6
E2	E	Yes	Adap	10	5	2.5	2.5	0.0	1	8.0	6	0.08	1.0	1–100	−1.6
EN1	E	No	Adap	10	5	2.5	4.3	0.5	1	8.0	6	–	–		–
EN1τ	E	No	Adap	10	5	2.5	4.3	0.5	1	8.0	$6+30e^{-t_{1.5}}$	–	–		–
EHR2	EHR	Yes	Adap	10	5	2.5	2.5	0.0	1	8.0	6	0.08	1.0	1–100	−1.6
C1	C	Yes	Adap	10	5	1.5	4.3	0.5	1	8.0	6	0.08	1.0	1–100	−1.6
C2	C	Yes	Adap	10	5	2.5	2.5	0.0	1	8.0	6	0.08	1.0	1–100	−1.6
CN1	C	No	Adap	10	5	1.5	4.3	0.5	1	8.0	6	–	–		–
S1f	S	Yes	Fix	10	5	1.5	4.3	0.5	1	8.0	6	0.08	1.0	1–100	−1.6
S2	S	Yes	Adap	10	5	2.5	2.5	0.0	1	8.0	6	0.08	1.0	1–100	−1.6
SN1	S	No	Adap	10	5	1.5	4.3	0.5	1	8.0	6	–	–		–
F1	F	Yes	Adap	10	5	1.5	4.3	0.5	1	8.0	6	0.08	1.0	1–100	−1.6
F1l	F	Yes	AdapLi	10	5	1.5	4.3	0.5	1	8.0	6	0.08	1.0	1–100	−1.6
F2	F	Yes	Adap	10	5	2.5	2.5	0.0	1	8.0	6	0.08	1.0	1–100	−1.6
F2l	F	Yes	AdapLi	10	5	2.5	2.5	0.0	1	8.0	6	0.08	1.0	1–100	−1.6
F2l$\zeta-$	F	Yes	AdapLi	10	5	2.5	2.5	0.0	1	8.0	6	0.04	1.0	1–100	−1.6
F3n	F	Yes	No	10	5	1.5	3.0	0.5	1	8.0	6	0.08	1.0	1–100	−1.6
F3n$\zeta-$	F	Yes	No	10	5	1.5	3.0	0.5	1	8.0	6	0.04	1.0	1–100	−1.6
FN1	F	No	Adap	10	5	1.5	4.3	0.5	1	8.0	6	–	–		–
FN1l	F	No	AdapLi	10	5	1.5	4.3	0.5	1	8.0	6	–	–		–
FN2	F	No	Adap	10	5	2.5	2.5	0.0	1	8.0	6	–	–		–
FN2n	F	No	No	10	5	2.5	2.5	0.0	1	8.0	6	–	–		–
J1	J	Yes	Adap	10	5	1.5	4.3	0.5	1	8.0	6	0.08	1.0	1–100	−1.6
J2	J	Yes	Adap	10	5	2.5	2.5	0.0	1	8.0	6	0.08	1.0	1–100	−1.6
JN1	J	No	Adap	10	5	1.5	4.3	0.5	1	8.0	6	–	–		–
JHR2	JHR	Yes	Adap	10	5	2.5	2.5	0.0	1	8.0	6	0.08	1.0	1–100	−1.6
G1	G	Yes	Adap	10	5	1.5	4.3	0.5	1	8.0	6	0.08	1.0	1–100	−1.6
G2	G	Yes	Adap	10	5	2.5	2.5	0.0	1	8.0	6	0.08	1.0	1–100	−1.6
GN1	G	No	Adap	10	5	1.5	4.3	0.5	1	8.0	6	–	–		–
GN1l	G	No	AdapLi	10	5	1.5	4.3	0.5	1	8.0	6	–	–		–

3.2 A resolution study

Fig. 3 shows the vertical density profiles at $R = 8$ kpc of three models that contain neither GMCs nor gas and differ only in the number N of particles used to represent the dark halo. Model YLHN1f has only 1 million halo particles and as a consequence its disc is distinctly thicker and hotter than the disc of model YN1f, which has 5 million particles in its dark halo. This difference between the two discs is clearly attributable to unphysical scattering of disc particles by halo particles. If we go to model YHHN1f, which has 25 million particles in its halo, the resulting disc is only marginally thinner than the disc in YN1f.

Fig. 4 shows an analogous plot for three models that all contain GMCs but differ in the number of particles representing their dark haloes and discs. YLR1 has 2 million particles in the halo and 2 million particles in the final disc, Y1 has 5 million particles each

Table 4. Models that contain gas. All these models have $t_f = 10$ Gyr, $M_f = 5 \times 10^{10}$ M$_\odot$, type 1 SFR, $t_{SFR} = 8$ Gyr and $\sigma_0 = 6$ km s^{-1}. The quantities given in columns 1–11 here are defined in the caption to Table 2. Columns 12 and 13 give values for the gas-mass fraction f_g and the sound speed c_s. Models that contribute to a figure have bold names.

(1) Name	(2) ICs	(3) GMCs	(4) Cutoff	(5) $h_{R,i}$ (kpc)	(6) $h_{R,f}$ (kpc)	(7) ξ	(8) ζ	(9) α	(10) $M_{low\text{-}up}$ (10^5 M$_\odot$)	(11) γ	(12) f_g	(13) c_s (km s^{-1})
YGN1	YG	No	Adap	1.5	4.3	0.5	–	–		–	0.1	10
YGN1c2	YG	No	Adap	1.5	4.3	0.5	–	–		–	0.1	20
YGN1c2g2	YG	No	Adap	1.5	4.3	0.5	–	–		–	0.2	20
YGN1c2g3	YG	No	Adap	1.5	4.3	0.5	–	–		–	0.3	20
YGN3c2g2	YG	No	Adap	1.5	3.0	0.5	–	–		–	0.2	20
YG1	YG	Yes	Adap	1.5	4.3	0.5	0.08	1.0	1–100	−1.6	0.1	10
YG1c2	YG	Yes	Adap	1.5	4.3	0.5	0.08	1.0	1–100	−1.6	0.1	20
YG2g2	YG	Yes	Adap	2.5	2.5	0.0	0.08	1.0	1–100	−1.6	0.2	10
EG2	EG	Yes	Adap	2.5	2.5	0.0	0.08	1.0	1–100	−1.6	0.1	10
FG2f	FG	Yes	Fixed	2.5	2.5	0.0	0.08	1.0	1–100	−1.6	0.1	10

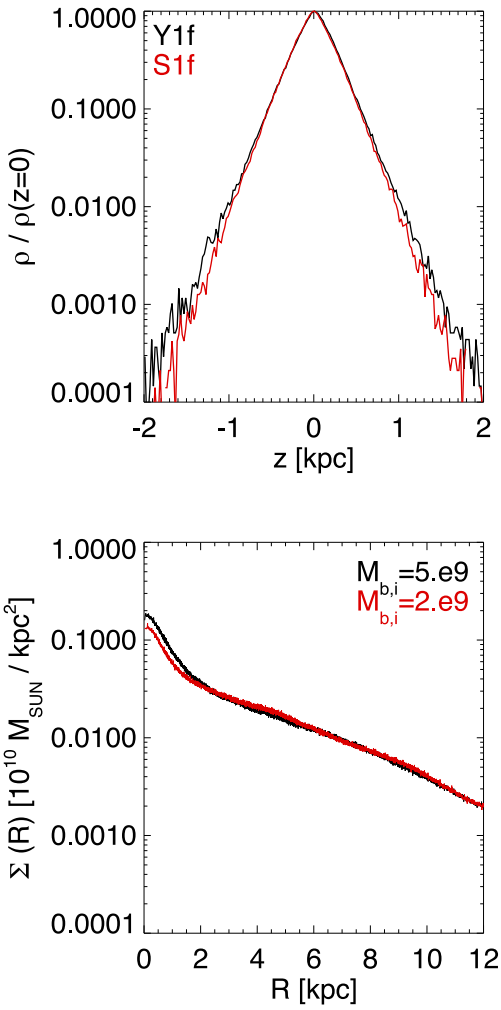

Figure 2. Comparison of models Y1f and S1f, which differ only in that the IC of S1f has only 40 per cent of the stellar mass of Y1f's IC. Top: vertical stellar density profile $\rho(z)$ at $R = 8$ kpc. Bottom: face-on stellar surface density profile $\Sigma(R)$.

in halo and final disc and YHR1 has 15 million particles each. Although the simulation with most particles (YHR1) clearly has the thinnest disc, the three profiles do not differ much. In particular, the differences are much smaller than that between the profiles

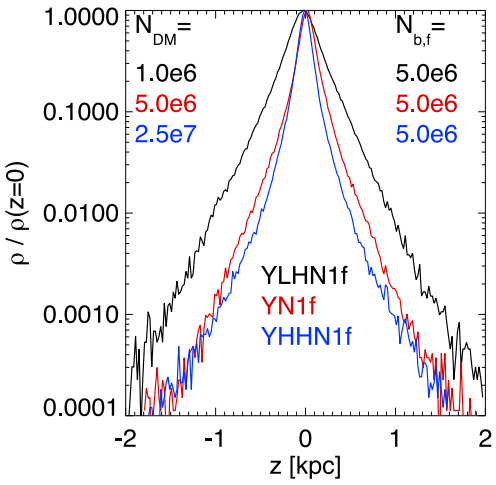

Figure 3. Vertical density profiles at $R = 8$ kpc of the stars of models YLHN1f, YN1f and YHHN1f. These models differ only in the number N of particles used to represent the standard $M = 10^{12}$ M$_\odot$ dark halo: $N = 1$, 5 and 25 million for YLHN1f, YN1f and YHHN1f, respectively. None of these models includes GMCs or gas. These results are presented at $t = 9.3$ Gyr, the last available output time for YHHN1f.

plotted in Fig. 3 for models without GMCs. We conclude that when more than a couple of million particles are used to represent the halo, spurious two-body heating of the disc is swamped by physical heating by GMCs and is consequently not a practical concern.

4 BASIC RESULTS

In this section, we summarize the most important lessons learnt from simulations that employ the standard dark halo, being the halo predicted for our Galaxy by concordance cosmology. In each subsection, we explicitly mention only a small subset of models that illustrate the relevant findings, but all models have been analysed in the same way as the cited models, and the models not mentioned are consistent with the stated findings. Further analysis will be presented in future papers.

4.1 Effectiveness of GMC heating

A remarkable feature of Fig. 4 is that the vertical profiles of all three models at $R = 8$ kpc are strikingly straight, implying that GMC

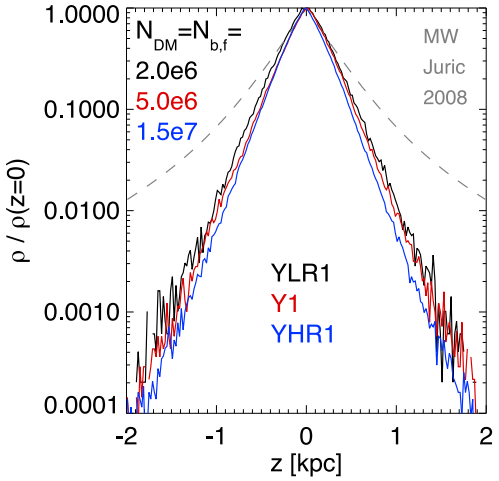

Figure 4. As Fig. 3 but showing models YLR1, Y1 and YHR1, which contain GMCs and differ only in the numbers of particles used to represent halo and stars: $(N_{\rm DM}, N_{\rm b,f}) = (2, 2), (5, 5)$ and $(15, 15) \times 10^6$ for YLR1, Y1 and YHR1, respectively. The grey dashed lines show the vertical profile of the Galactic disc at the solar radius R_0 determined by Jurić et al. (2008).

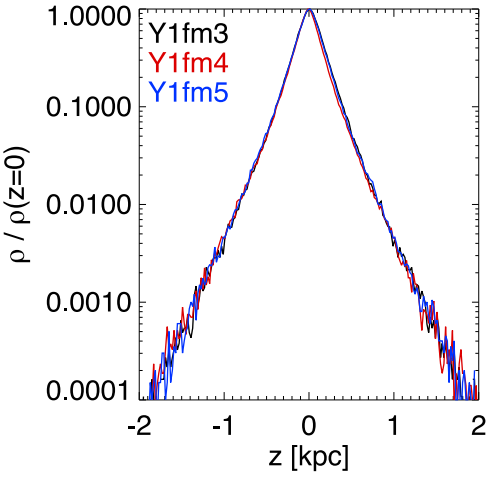

Figure 5. The vertical stellar density profiles at $R = 8$ kpc of three models, Y1fm3, Y1fm4 and Y1fm5, that differ only in their GMC mass functions. Their mass functions nevertheless yield the same effective mass (equation 15) and as a consequence the models' vertical profiles are indistinguishable.

heating produces an accurately exponential vertical profile out to at least $z = 2$ kpc. Another remarkable fact is that the exponential scaleheights of these profiles ($h_z = 210$–235 pc) are comparable to but smaller than the measured scaleheight of the Galaxy's thin disc.

The grey dashed lines in Fig. 4 show the vertical profile of the Galactic disc at the solar radius R_0 in the analysis of Jurić et al. (2008) of the Sloan Digital Sky Survey (SDSS) photometry. This profile is shown in several figures throughout the paper and represents a bias-corrected model fit to the data of the form

$$\rho(z, R = 8\,\mathrm{kpc}) = \rho_0[\exp(-|z|/h_{\rm thin}) + f\exp(-|z|/h_{\rm thick})]. \quad (14)$$

Jurić et al. (2008) find $h_{\rm thin} = 300$ pc and $h_{\rm thick} = 900$ pc with 20 per cent uncertainty each and $f = 0.12$ with 10 per cent uncertainty.

We see that GMCs produce a disc that has a suitable scaleheight near the plane ($|z| \lesssim 0.5$ kpc) but completely fails to fit the data at greater heights because it lacks a thick-disc component.

The heating efficiency of GMCs depends on the contribution of the GMCs to the disc's surface density, which is controlled by the SFR and the efficiency parameter ζ – smaller values of ζ imply a higher surface density from GMCs at a given SFR. The heating efficiency also depends on the mass spectrum of the clouds. Jenkins & Binney (1990) gave an analytic argument that the heating efficiency of clouds depends on the mass function $N(m)$ through the effective mass

$$\mathcal{M} \equiv \frac{\int \mathrm{d}m\, m^2 N(m)}{\int \mathrm{d}m\, m N(m)}. \quad (15)$$

In Fig. 5, we plot the vertical profiles of three models Y1fm3, Y1fm4 and Y1fm5 at $R = 8$ kpc, which all have effective mass $\mathcal{M} = 10^6\,\mathrm{M}_\odot$. We see that the density profiles of these models coincide perfectly, as Jenkins & Binney (1990) predicted.

In Fig. 6, we explore the importance of concentrating GMCs in spiral arms by increasing the parameter α in equation (12) from zero (no concentration) to 2 ($\rho_{\rm GMC} \propto \rho_{\rm ys}^2$). As expected, concentrating GMCs into spirals (as seen in observations; e.g. Schinnerer et al. 2013) enhances the heating efficiency of GMCs by enabling them to act cooperatively. The effect is, however, small. We will henceforth adopt $\alpha = 1$.

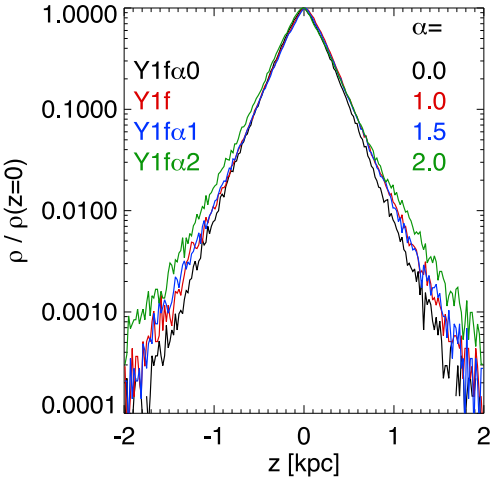

Figure 6. Vertical stellar density profiles at $R = 8$ kpc of four models with different values of the parameter α that controls the extent to which the density of GMCs is enhanced by spiral structure (equation 12). Concentrating GMCs (larger α) into spiral arms enhances their heating efficiency, but the effect is small.

GMC heating is very effective at early times, because then (i) the SFR is high so the surface density of GMCs is large, and (ii) an individual GMC represents a larger fraction of the disc mass than it does today, when the disc is 10 times more massive than it was at $z = 2$. An important effect of prompt heating by GMCs is to delay, and in extreme cases cancel, the formation of a bar. Fig. 7 illustrates this point by showing surface density maps at four times for models YN1 (top), which has no GMCs, and its GMC possessing partner Y1. YN1 has a prominent bar already at 4 Gyr while in Y1 the bar appears first at 7 Gyr. Moreover, at 10 Gyr the bar is longer in YN1 than in Y1.

To assess the strength and length of bars in our simulations, we use equation (9) to determine the profile of the $m = 2$ Fourier amplitude A_2. We define a bar as a central structure with $\ln(A_2) > -1.5$ and its length $L_{\rm bar}$ as the radius where A_2 drops below this value. To determine the formation time of a bar, we plot $L_{\rm bar}$ as a function of time t and look for the earliest time after which $L_{\rm bar}$

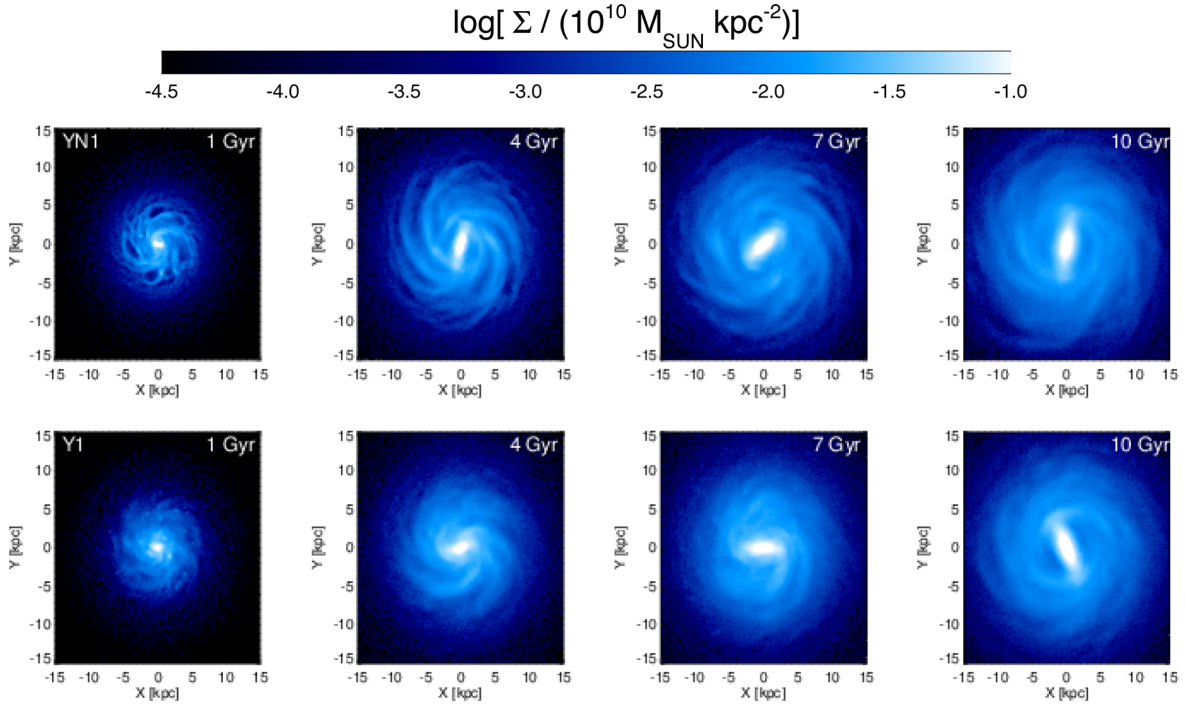

Figure 7. Face-on stellar surface density $\Sigma(x, y)$ pictures of models YN1 and Y1 at $t = 1, 4, 7, 10$ Gyr.

is continuously larger than 1 kpc. Note that bars can dissolve and reform.

The MW bar has a distinct 'X' shape (Wegg & Gerhard 2013), as have many bars in edge-on galaxies. This is the result of the buckling instability (Combes et al. 1990), which occurs when the bar has acquired a critical strength. As far as the bars in our simulations are concerned, we find that in the absence of GMCs, or in models with low GMC effective mass $\mathcal{M}$, all bars buckle. If we consider different Y1 models irrespective of the cutoff prescription and define an efficiency parameter $\chi = \mathcal{M}/(10^6 \zeta\, \mathrm{M}_\odot)$, all models with $\chi < 14$ buckle. For $14 < \chi < 40$, we find both buckled and unbuckled bars, as the evolution of bar length and strength is to some degree stochastic (Sellwood & Debattista 2009) and the detailed evolution history of a model bar decides if a bar buckles or not. All models with $\chi > 40$ have weak bars, which do not buckle. The bars in models YN1 and Y1 shown in Fig. 7 have both buckled.

4.2 AVR

In the left-hand panels of Fig. 8, we compare σ_z (upper panel) and σ_R (lower panel) at $R = 8$ kpc as a function of stellar age τ at the endpoints of four models that differ only in whether or not they have GMCs (Y1 and YG1 do) and whether or not they have gas (YG1 and YGN1 do). We overplot in grey $\sigma_i(\tau)$ as measured for the Snhd by Casagrande et al. (2011). For these points, which are shown in several plots throughout the paper, only stars with relatively low 1σ age errors σ_τ are considered ($\sigma_\tau < 1$ Gyr or $\sigma_\tau/\tau < 0.25$). Moreover, stars with [Fe/H] < -0.8 or $V < -150\,\mathrm{km\,s^{-1}}$ are excluded to avoid contamination with halo stars.

The major uncertainties in the Snhd AVR for very old stars are connected to the uncertainties in excluding halo stars. Fig. 17 in Casagrande et al. (2011) illustrates this and shows that these uncertainties are ∼10 per cent. For young stars, uncertainties in the AVR derive from the age errors and the intrinsic shape of the AVR. Generally, the age uncertainty in the Casagrande et al. data is substantial and can significantly modify $\sigma(\tau)$ by contamination from neighbouring age bins. Moreover, the Geneva Copenhagen Survey (GCS) selection function excludes very blue stars and thus removes stars from the sample that could be safely identified as very young ($\tau \lesssim 1$ Gyr) objects. It also favours greatly stars with ages $\tau \sim 2$ Gyr, so that the lowest age bins are dominated by stars with age underestimates from that peak in the age distribution. One can use the bluest *Hipparcos* stars for which Aumer & Binney (2009) find $\sigma_z = 5.5\,\mathrm{km\,s^{-1}}$ and $\sigma_R = 8\,\mathrm{km\,s^{-1}}$ to estimate the dispersions of the youngest stars, which are clearly smaller than what we find from the youngest GCS stars. However, these stars may be kinematically biased as they belong to a low number of moving groups of young stars. Also, these blue stars have associated ages which are smaller than the typical age errors of observed stars and smaller than the bin sizes used for the simulations, so that neither for the simulations nor for observations we would expect to recover the velocity dispersion of this population.

To attenuate some of these uncertainties, the model curves plotted in Fig. 8 have been adjusted to allow for the impact of the Casagrande et al. age uncertainties and biases (Aumer et al., in preparation). Selection function effects for the bluest stars are, however, not taken into account. Thus, our simulations overestimate the number of intrinsically very young stars and hence underestimate the relative contamination with age underestimates. This explains why our model dispersions are lower than observed dispersions at $\tau \lesssim 1$ Gyr. As the stars examined by Casagrande et al. were all observed close to the Galactic mid-plane, for our models we only consider stars at low altitudes $|z| < 100$ pc. Furthermore, the simulations only cover 10 Gyr and we assign ages of 10–11 Gyr to the IC particles. So at ages $\tau > 11$ Gyr, the simulation curves only show upscattered younger stars, whereas the Snhd data also contain stars which are actually older than 11 Gyr.

Considering these complications, we find that the models with GMCs provide moderate fits to the data for $\sigma_z(\tau)$, while the models without GMCs have σ_z too small.

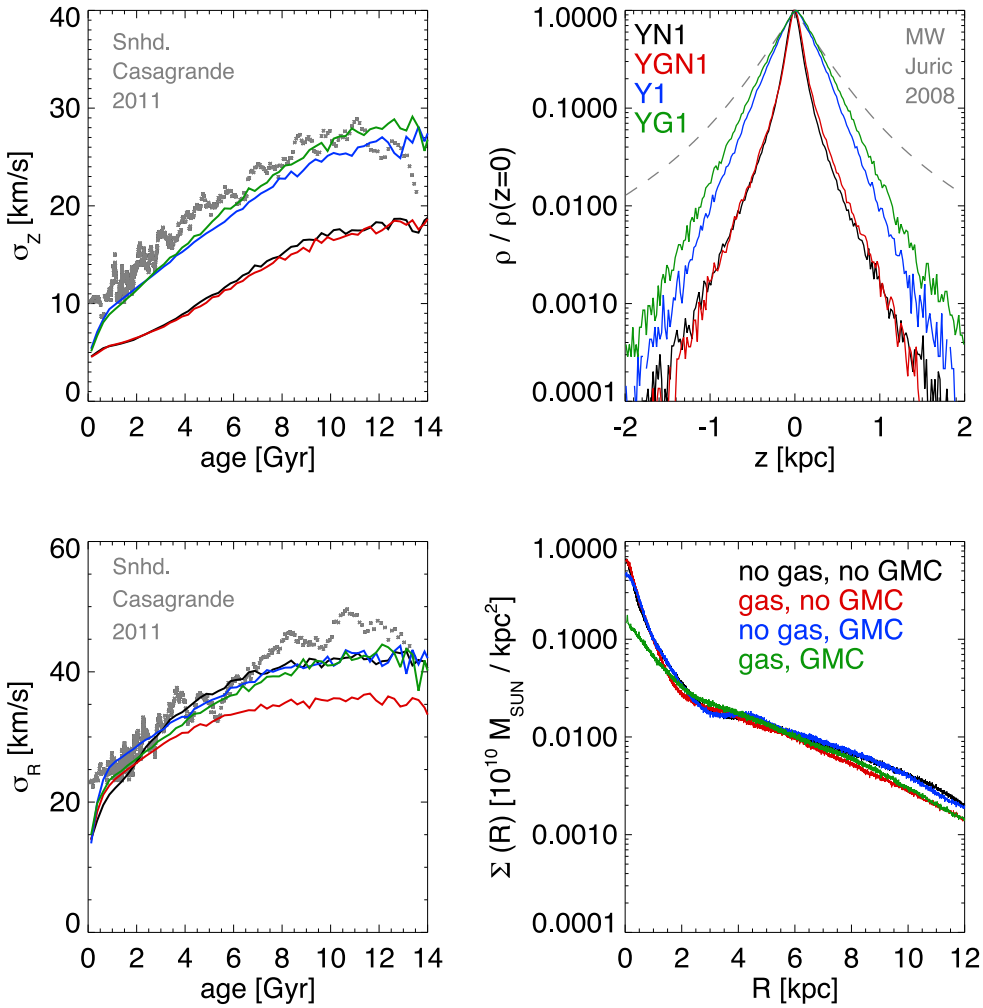

Figure 8. A comparison of models YN1 (no gas, no GMCs), YGN1 (gas, no GMCs), Y1 (GMCs, no gas) and YG1 (gas, GMCs). Top right: vertical stellar density profile $\rho(z)$ at $R = 8$ kpc. Bottom right: radial stellar surface density profiles $\Sigma(R)$. Left-hand panels: age–velocity dispersion (σ_z upper, σ_R lower panel) relations of stars at $R = 8$ kpc. The grey dots show data for the Snhd from Casagrande et al. (2011) and the model curves have been adjusted to simulate the impact on measured dispersions of the uncertainties and biases in the ages determined by Casagrande et al.

The absence of GMCs from YN1 does not stop this model providing a moderate fit to the data for $\sigma_R(\tau)$, but adding gas to this model to make YGN1 does push $\sigma_R(\tau)$ well below the data. We explain this phenomenon in the next section. The fact that GMCs are not needed to explain observed $\sigma_R(\tau)$, but are required to explain $\sigma_z(\tau)$ confirms Carlberg (1987), who argued that heating by spirals and bars can explain the in-plane dispersions, but GMCs are needed to explain the vertical heating.

4.3 Impact of gas

The right-hand panels of Fig. 8 compare vertical stellar profiles at $R = 8$ kpc (upper panel) and radial stellar profiles (lower panel) of the four models YN1, YGN1, Y1 and YG1, discussed in the last section. The black and red vertical profiles for the GMC-free models YN1 and YGN1 are essentially identical (as are their curves for $\sigma_z(\tau)$), so on its own, gas is not an effective heating agent. Since the green curves for YG1 lie above the blue curves for Y1 in the upper panels of Fig. 8, we conclude that gas *does* enhance the heating efficiency of GMCs. This is presumably because a GMC particle attracts a wake of gas particles, and this wake increases the GMC's effective mass. In Fig. 8, the vertical profiles of the models with GMCs are almost perfectly exponential with scaleheights $h_z = 225$ (no gas) and 253 pc (with gas).

The radial profiles shown in the lower-right panel of Fig. 8 comprise a steep section for $R < 2$ kpc associated with the bar, flattening into an extended outer section for the disc. Model YG1, with both gas and GMCs, has a distinctly less prominent bar section than the other three models. We have already seen that GMCs tend to weaken bars. The profile for YG1 signifies that gas also weakens bars. Gas can weaken bars in three ways. One is simply by enhancing the effectiveness of GMC heating. Another is by blowing mass out of the central galaxy, thus weakening the disc's self-gravity. The third way gas can weaken a bar is by carrying angular momentum over the bar's corotation resonance and then surrendering it to the bar: when a bar acquires angular momentum, it becomes faster, shorter and weaker – and conversely when it loses angular momentum to the dark halo. The first process will not be active in model YGN1 that has gas but no GMCs, and the radial profile in Fig. 8 indicates that the bar in this system is significantly shorter than that in YN1, which has neither gas nor GMCs. Thus, on its own gas does not prevent bar formation, but it does limit bar growth. Acting in concert with GMCs, gas can strongly delay bar formation.

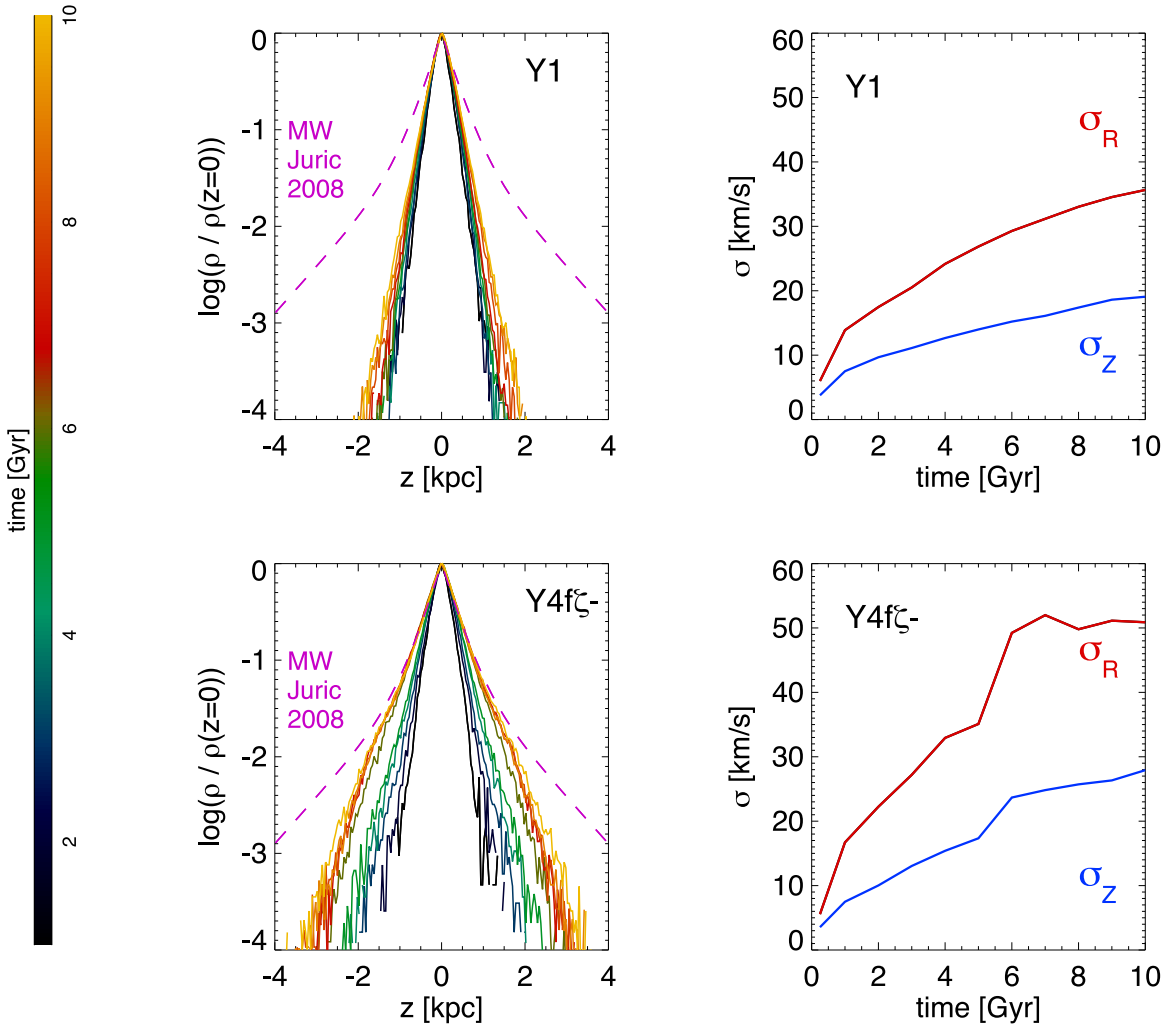

Figure 9. Right-hand panels: velocity dispersions σ_z and σ_R at $R = 8$ kpc as a function of time in models Y1 and Y4f$\zeta-$. Left-hand panels: time evolution of vertical stellar density profiles at $R = 8$ kpc. The colour bar at extreme left shows the time encoding.

Note that the radial profiles show only stellar mass. As gas models have a fraction of their disc mass in gas, their overall stellar surface density is lower. Still, at large R the radial profiles of the two models without gas fall off less steeply than the profiles of the models with gas. That is, adding gas reduces the scalelength of the final disc. Presumably, this is partly a side effect of reducing the strength of the bar, and partly caused by viscous inflow of gas through the disc.

4.4 Vertical profiles and dispersions over time

We have already shown that most models with GMCs show exponential vertical profiles which lack thick components. Among our Y models, we find ∼five models which have noticeable wings at $|z| \gtrsim 1$ kpc in their vertical density profiles, suggestive of a thick disc. Apart from Y3f, which has a very mild wing, all these models share with Y4 a growth history in which the scalelength for star insertion rises only to $h_{R,\mathrm{f}} = 2.2$ kpc, so the disc is fed compactly. Model Y4f$\zeta-$ stands out amongst these models in having a vertical profile that rather nearly matches that of our Galaxy up to $|z| = 2$ kpc, but still falls off much more steeply at higher altitudes. Apart from a compactly fed disc, Y4f$\zeta-$ has a fixed inner cutoff and an SF efficiency of only 4 per cent, so it combines strong GMC heating with strong spiral structure due to the compact feeding.

In this section, we compare Y4f$\zeta-$ to one of the standard GMC models, Y1, which has inside-out growth to $h_{R,\mathrm{f}} = 4.3$ kpc, SF efficiency $\zeta = 0.08$ and an adaptive cutoff, to understand the origin of the different vertical profiles. In the right-hand panels of Fig. 9, we plot the vertical component of velocity dispersion for stars of all ages at $R = 8$ kpc in both models. In Y1 σ_z grows steadily, while in Y4f$\zeta-$ steady growth of σ_z is interrupted by a jump at $t \sim 5$ Gyr.

The left-hand panels of Fig. 9 show the vertical density profiles of these models at $R = 8$ kpc at several times between 1 (black) and 10 Gyr (yellow). Notwithstanding the steady growth in σ_z, the vertical profile of Y1 changes remarkably little. This is in part because heating by GMCs is offset by adiabatic contraction as the disc gains mass, and in part because the mid-plane density is being constantly increased by the addition of star particles. The sudden increase in σ_z at $t \sim 5.5$ Gyr *does* cause the vertical profile of Y4f$\zeta-$ to change significantly, because the sudden increase in σ_z is not offset by a sudden increase in surface density or enhancement of density at $z = 0$.

The sudden increase in σ_z is caused by a strong and extended $m = 3$ mode developing in its disc, followed by a large bar structure. These non-axisymmetric structures cause strong radial redistribution of stars and lead to final scalelengths of the disc that are significantly larger than the compact input scalelengths. We find

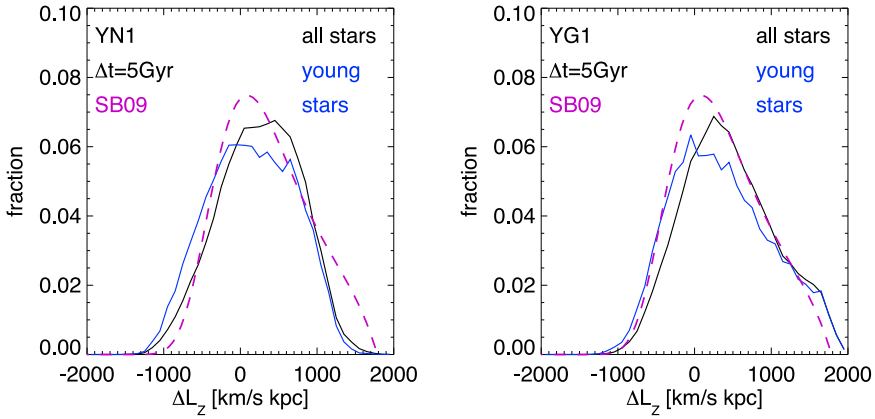

Figure 10. Plots of changes in L_z in the last 5 Gyr for two samples of stars selected to have $L_z = L_{z,\mathrm{circ}}(8\,\mathrm{kpc}) \pm 100\,\mathrm{kpc\,km\,s^{-1}}$ at $t = t_\mathrm{f}$ in models YN1 (left) and YG1 (right). The black curves are for all stars that are more than 5 Gyr old, while the blue curves are for stars with ages 5–6 Gyr, so ΔL_z is the change in their angular momentum since they were young. Also plotted as a broken line is the corresponding distribution inferred by SB09a from the chemical composition of Snhd.

that using a fixed cutoff for Y4 models leads to more extended non-axisymmetric structures and thus more strongly thickened discs, than an adaptive cutoff. For the Y models with milder thick wings, we find that their thick components arise from similar processes of smaller magnitude.

4.5 Radial migration

When a star is scattered by a non-axisymmetric structure across the structure's corotation resonance, its angular momentum changes appreciably without any increase in the eccentricity of its orbit (Sellwood & Binney 2002). Since a change in L_z corresponds to a change in the star's guiding-centre radius R_g, this process drives radial migration. Fig. 10 shows for two models, YN1 and YG1, histograms of the change $\Delta L_z \equiv L_z(10\,\mathrm{Gyr}) - L_z(5\,\mathrm{Gyr})$ in the angular momentum of stars which at $t = t_\mathrm{f}$ have angular momentum in the range $L_z = L_{z,\mathrm{circ}}(8\,\mathrm{kpc}) \pm 100\,\mathrm{kpc\,km\,s^{-1}}$. Here $L_{z,\mathrm{circ}} \equiv Rv_\mathrm{circ}(R)$ and these stars thus have $R_\mathrm{g} \approx 8\,\mathrm{kpc}$. The black curves include all stars older than 5 Gyr, while the blue curves are for stars with ages 5–6 Gyr, so ΔL_z is the change in their angular momentum since they were young.

Minchev & Famaey (2010) claim that bars can contribute to radial migration. Fig. 10, however, reveals that the histogram of ΔL_z values for a model, YN1, with one of the strongest bars shows a sharp drop at high positive ΔL_z. For young stars, this cutoff simply reflects the fact all such stars have started from near-circular orbits at $R > R_\mathrm{cut}(5\,\mathrm{Gyr}) = 3.3\,\mathrm{kpc}$, so stars now near $R_\mathrm{g} = 8\,\mathrm{kpc}$ have $\Delta L_z \lesssim v_\mathrm{circ} \times (8 - 3.3)\,\mathrm{kpc}$. Older stars could have reached $R_\mathrm{g} = 8\,\mathrm{kpc}$ from any radius in the disc, so the fact that their histogram of ΔL_z values shows the same cutoff implies that stars are not escaping from within the bar (which by construction extends to $R \sim R_\mathrm{cut}$). This conclusion is reinforced by the fact that a model such as YG1, which develops a short bar very late on, has a histogram of ΔL_z values that has a peak of comparable width to that of YN1, plus an extension at fraction $\sim$0.02 that reaches to values of ΔL_z that are $\sim$500 kpc km s^{-1} larger than those reached by the histogram for YN1. We conclude that in our simulations bars play a minor role for radial migration to $R = 8\,\mathrm{kpc}$.

SB09a showed that radial migration enables us to understand the chemical composition and widening age–metallicity relation of the Snhd in a natural way from basic chemical evolution. Metal advection by the inward directed galactic flow and (to a lesser degree) the faster and earlier SF make the inner regions of the galaxy significantly more metal rich than the outskirts. Radial migration brings those stars now to the Snhd on time-scales of a few Gyr, while those locally measured stars have only small differences in mean asymmetric drift versus metallicity. It should be noted that for the models shown in Fig. 10, $L_{z,\mathrm{circ}}(R = 8\,\mathrm{kpc}) \sim 1900\,\mathrm{km\,s^{-1}\,kpc}$, which means that the stars with the highest ΔL_z in model YG1 had very small L_z at $t = 5\,\mathrm{Gyr}$. So, radial migration can bring stars from the inner regions of a galaxy to the outer disc on cosmological time-scales. This has been indirectly inferred from observations of stars in the Snhd that are more metal rich than the Sun but old and yet not on highly eccentric orbits (Casagrande et al. 2011; Kordopatis et al. 2015).

SB09a used their chemodynamical evolution model to determine the required strength of radial migration. A parameter was used to control the width of the ΔL_z distribution, and by fitting their model to the local chemistry they could determine the optimum value of this parameter and thus predict the ΔL_z distribution. The magenta dashed curves in Fig. 10 show this prediction. The agreement between this predicted distribution and that measured in model YG1 (and many other models) is remarkable considering the different physical principles generating each distribution. In fact, the differences between the SB09a predictions and the models are smaller than the uncertainties for these comparisons arising from differences in e.g. radial density distributions or rotation curves – assumed in SB09a,b to be flat at $v_\mathrm{circ} = 220\,\mathrm{km\,s^{-1}}$.

The overwhelming majority of our Y models yield histograms of ΔL_z that are similar to one of those shown in Fig. 10 or are intermediate between these two cases. Models which have strong bars already in place at $t = 5\,\mathrm{Gyr}$ yield ΔL_z distributions like that of YN1. These include models without GMCs, such as YN1 and YN3 and models with $\zeta = 0.16$ and thus lower total GMC mass, such as Y1fζ+ or Y1fζ+m2. In the majority of Y models with GMCs, bars are weaker and form at later times (see also Section 4.1), but they show well-developed spiral structure and their distributions of ΔL_z are more similar to that of YG1. Hence, strong deviations from the predicted ΔL_z distribution of SB09a are rare. An unusually narrow histogram is produced by model Y2Mb−, which has an anomalously low-mass disc ($M_\mathrm{f} = 3 \times 10^{10}\,\mathrm{M_\odot}$) and lacks inside-out formation ($h_{R,\mathrm{i}} = h_{R,\mathrm{f}} = 2.5\,\mathrm{kpc}$). Models Y2Mb+, which has a higher disc mass, and Y4fζ−, which develops extended non-axisymmetric structures, show mildly wider ΔL_z distributions.

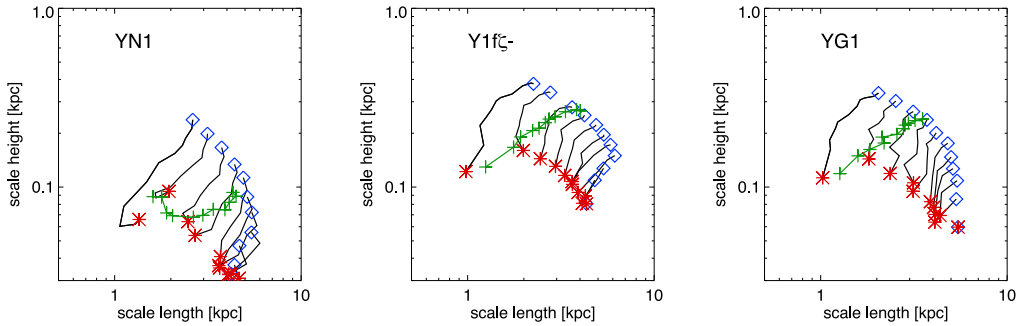

Figure 11. Each black curve shows fitted values of h_R and h_z to the spatial distribution of an almost coeval population at a series of times: a red star marks values at the earliest time (when ages lie in (0, 1) Gyr) and a blue diamond marks values during the last Gyr of the simulation. For h_R we consider the region $R = 6$–10 kpc and for h_z we use the vertical profile at $R = (8 \pm 1)$ kpc. In every case, the particles of the IC yield the curve at top left. Fits to the distribution of all stars, regardless of age, are marked by green crosses.

In non-standard models with halo F (see Section 5.2.1), very extended $m = 2$ structures can develop which can lead to noticeable excesses of stars at $\Delta L_z < 1000\,\mathrm{km\,s^{-1}}$ kpc (e.g. models FN1, F2l). For models with thick-disc ICs and GMCs (see Section 5.1), strong bars tend to form earlier than in Y models and thus a higher fraction of models, including e.g. Z1 and A1τ, show a sharp drop at high positive ΔL_z similar to YN1. A detailed discussion of the dependence of radial migration on the disc's evolution history is a topic for a future paper.

In contrast to the models of SB09b, where old, kinematically hot stars form a thick disc, our simulations do not develop thick discs. This arises from the modelling of the vertical heating applied in SB09b, which differs from our simulation in three respects. (i) The assumption of vertical energy conservation in SB09a was disproved by Solway, Sellwood & Schönrich (2012), who demonstrated that action rather than energy was conserved. (ii) SB09a used for each population a heating law that depends only on birth radius, while stars are heated throughout their trajectory through the galaxy. With a given heating law, this assumption exaggerates the difference between the final random velocities of stars born at small and large radii. (iii) SB09a assumed a fixed radial dependence of the heating to ensure constant scaleheight of the local populations. Preliminary examinations of our simulations however show less inner disc heating and also a different time dependence. A detailed discussion of heating rates will follow in a subsequent paper.

4.6 Scalelength growth

Each black curve in a panel of Fig. 11 shows the exponential scalelengths (h_R, h_z) recovered at different times for particles that were inserted in a time interval 1 Gyr long. Particles present in the ICs form the oldest cohort, and their curve lies at the upper-left end of the series of curves. The next oldest cohort is formed by particles added in the simulation's first gigayear, etc. Somewhat analogously, Bovy et al. (2012a) plotted a point in the (h_R, h_z) plane for each 'mono-abundance' population of the Galaxy, and found that the points of 'α-old' populations tended to lie above and to the left of the points of 'α-young' populations. In the spirit of that study, we determine h_z by fitting single exponentials to the distribution in z of particles that lie in the cylindrical shell 2 kpc wide around $R = 8$ kpc. We determine h_R by fitting single exponentials to the radial surface density profile of particles that lie at $R = 6$–10 kpc. Each cohort's red star shows (h_R, h_z) just after the birth of the cohort, and the blue diamond shows the values at the end of the simulation. Hence, the blue diamonds are what one might compare with the points of Bovy et al. (2012a).

The horizontal location of the red stars simply reflects the rule used to add particles. When a model has inside-out growth (e.g. Y1f$\zeta-$), the red stars march to the right, but in other cases (e.g. Y2) they do not. The vertical locations of red stars reflect the velocity dispersions of young stars, and they tend to move downwards over time because as the disc gains surface density, the velocity dispersion that can be acquired in ∼0.5 Gyr allows particles to move less far from the plane. For nearly every cohort in nearly every model, the scalelengths (h_R, h_z) at birth are significantly smaller than their values at the end of the simulation. Exceptions to this rule are models such as Y2Mb− that have anomalously low-mass discs and consequently develop only weak spiral structure, so that h_z increases at roughly constant h_R.

In Fig. 11, the leftmost panel for YN1 is notable for the small values of h_z that arise because this simulation has no GMCs. The middle panel for Y1f$\zeta-$ has more realistic values of h_z because it has GMCs. The panel on the extreme right, for YG1, shows somewhat less growth in h_R because the introduction of gas has weakened the bar.

The green crosses in Fig. 11 show the values of (h_R, h_z) obtained by fitting all stars present at each epoch, regardless of their age. When there are no GMCs, h_R grows but h_z does not (left-hand panel), while both scalelengths grow in concert when GMCs are present.

In Fig. 12, we show the resulting surface density profiles from five models, which only differ in their radial growth history $h_R(t)$. They all grow with time as $t^{\xi=0.5}$. We find that the three compact models Y2, Y3 and Y4 have almost indistinguishable radial profiles. The more extended models Y5 and Y7 have smaller central regions of enhanced surface density, reflecting shorter bars. In these models, the bars are shorter because surface densities are lower. At $R \sim$ 3–7 kpc, all profiles are almost parallel, i.e. have similar output scalelengths despite the different input scalelengths. This radial redistribution is caused by non-axisymmetric disc structures. The more compact models have down-turning breaks at $R \sim 8$ kpc, whereas Y5's profile turns down at $R \sim 10$ kpc and Y7 is exponential out to $R > 30$ kpc.

Model Y1 is not shown because it is intermediate between Y5 and Y7. Model Y6 has a different time dependence of radial growth ($\xi = 0.2$), but otherwise the same parameters as Y3, and it hardly differs from Y3. In Y1f, Y3f and Y4f, the use of fixed rather than adaptive cutoffs makes the zones of equal scalelengths broader

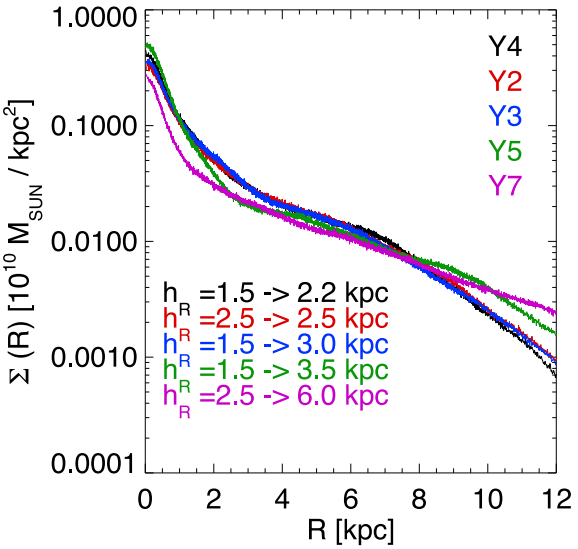

Figure 12. Face-on stellar surface density profiles $\Sigma(R)$ for models, which differ only in their radial growth history $h_R(t)$. They all grow with time as $t^{0.5}$.

($R \sim 3$–9 kpc) and the radial breaks in the profiles of Y3f and Y4f move outwards to $R \sim 9$–10 kpc.

4.7 Flaring of discs

It is generally accepted that the vertical profiles of disc galaxies are very constant radially (van der Kruit & Searle 1982). The left-hand panels of Fig. 13 examine this in the case for our final models. Lines of various colours show profiles from $R = 2$ kpc (black) to $R = 16$ kpc (dark yellow).

Model Y1 has a buckled bar, which causes a mildly thicker, non-exponential profile in the bar region. In all other regions, the vertical profiles are exponential and almost indistinguishable. As described in Section 4.4, the majority of our Y models with GMCs have single-exponential vertical profiles. Model Y1 is typical of this class. As discussed in Section 4.1, not all of these models have buckled bars. In models without a buckled bar (e.g. Y2, Y1$\zeta-$), the vertical profile is constant throughout the whole radial range.

As discussed in Section 4.4, a minority of our Y models have deviations from single-exponential vertical profiles in the form of thick wings. Model Y4f$\zeta-$ is the most extreme of these models and thus behaves very differently in Fig. 13. At inner radii the profile is single exponential, as the bar has not buckled. The profile becomes significantly thicker with increasing R, and thickness increases continuously with radius. The thicker profiles are not double exponential, but rather flatten at $|z| = 1$ kpc and then fall off steeply at higher altitudes. Models with milder thick wings, such as Y4f, also show flaring, but the effect is considerably milder than for Y4f$\zeta-$.

Minchev et al. (2015) using cosmological simulations by Aumer et al. (2013) and Martig et al. (2014) recently claimed that all mono-age populations of stars should have vertical profiles flaring with radius. In this picture, inside-out formation keeps the total vertical profile roughly constant with radius and the thick-disc stars at a given altitude become younger with increasing radius. In the right-hand panels of Fig. 13, we show how the median altitude $|z|$ changes with radius R for stars in age bins between 0 (black) and 11 Gyr (IC stars, dark yellow).

We notice that at all radii the median $|z|$ increases monotonically with age for both models as a consequence of the monotonically increasing AVRs. Only the oldest component of the outer disc of Y1 behaves differently. This population was initially very compact and at 10 Gyr still has a very low density in the outer disc. This brings along a peculiar population of very eccentric orbits, which can reach the outer regions, but have less-than-average vertical action.

The youngest stars always flare, which results from the constant input vertical velocity dispersion and the reduced vertical force at lower surface densities in the outer disc. In Y1 bar buckling causes all populations older than 1 Gyr to be thicker in the inner disc. Outside the bar region, all populations except the IC stars show mild flaring. In models without a buckled bar, the median $|z|$ of these populations would decrease monotonically towards $R = 0$.

Model Y4f$\zeta-$, which has a thick vertical structure, shows strong flaring for the old and intermediate-age components: the median $|z|$ increases by factors in excess of 2.

5 NON-STANDARD MODELS

We have seen that models with a generous supply of massive GMCs and a standard disc and a standard dark halo yield quite realistic bars and thin discs under a range of reasonable assumptions regarding how particles are added to the disc. However, we have been conspicuously unsuccessful in generating a thick disc. A burning question is whether our failure to create a realistic thick disc arises from an inappropriate parametrization of disc growth or a poor choice of parameters. And if our failure cannot be ascribed to either of these causes, how were thick discs made?

5.1 A thick disc from the ICs?

Since dynamics is not generating enough stars with large vertical actions, we add such stars by hand. First we just add them to the ICs by including a bulge (IC C) or a massive and extended thick disc (ICs Z, A, E). The upper panel of Fig. 14 shows the vertical density profiles at $R = 8$ kpc and illustrates the outcome of these experiments. The only model to come near to the goal of generating an adequate thick disc is E2, which starts from a disc with scalelengths $(h_{R,\rm disc}, z_{0,\rm disc}) = (2.5, 1.2)$ kpc that is three times more massive ($M_{\rm b,\,i} = 1.5 \times 10^{10}$) than standard, so at birth we are endowing this model with something very like the Galaxy's current thick disc.

The essential challenge of matching the observed density of stars 1–2 kpc above the Sun is endowing the IC with enough stars with large values of the vertical action J_z. The IC disc is relatively low mass, so the vertical gravitational force it provides is not large, and stars with the required values of J_z must rise high above the mid-plane. Hence, the structure furnished by the ICs has to be fat. The structure also has to have a significant extent radially because it does not grow much radially during the formation of the thin disc – as the mass inside a circular orbit grows, the orbit's radius decreases.

In addition to not providing enough stars in the final model at $|z| = 2$–4 kpc, model E2 has a thin disc that is too thick, and a bar that is too long (∼6 kpc). Therefore, in the lower panel of Fig. 14, we report the results of varying the way particles are added to ICs A and E. These include (i) giving particles an initial velocity dispersion σ_0 that declines from 36 km s^{-1} to the standard value 6 km s^{-1} on a characteristic time-scale 1.5 Gyr (models A2τ, E1τ, EN1τ), (ii) letting the scalelength for addition grow (from $h_{R,\rm i} = 2.5$ kpc to $h_{R,\rm f} = 4.3$ kpc in E1 and E1τ and EN1τ rather than fixing it at 2.5 kpc in E2) and (iii) excluding GMCs (EN1τ).

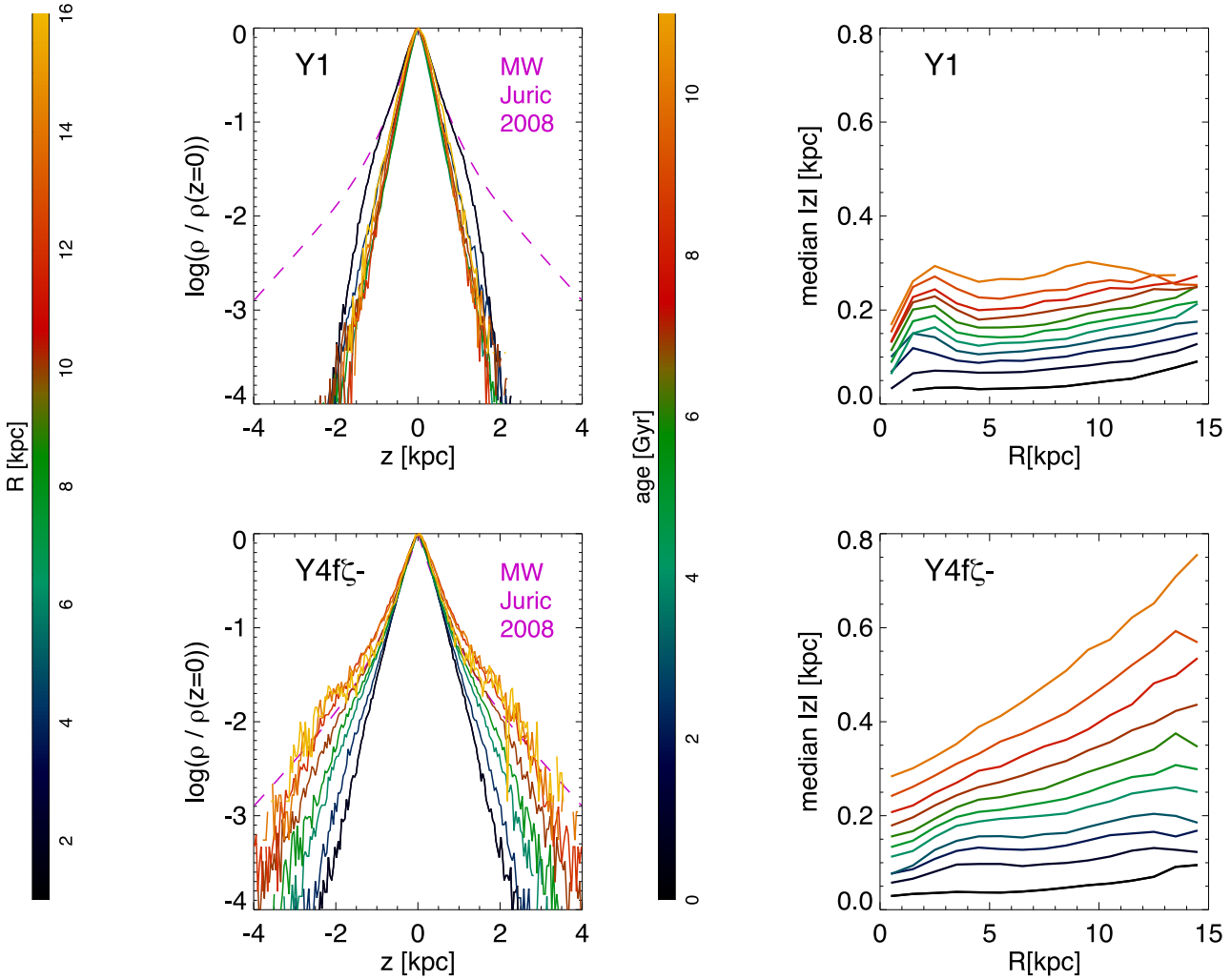

Figure 13. Left-hand panels: radial dependence of the vertical profiles of models Y1 and Y4f$\zeta-$ between $R = 2$ (black) and 16 kpc (dark yellow) as indicated on the colour bar at extreme left. Right-hand panels: the median altitude over the mid-plane $|z|$ of mono-age populations in models Y1 and Y4f$\zeta-$ as a function of radius R. Here colour encodes age between 0 (black) and 11 Gyr (dark yellow) as indicated on the central colour bar.

E1τ comes closest to the promise shown by E2, but again provides far too few stars at $|z| = 1$–4 kpc. It produces a thin disc in better agreement with the data as it has a shorter bar of length ∼4.5 kpc that compares well with that in the MW. Assuming $\sigma_0 \sim 36\,\mathrm{km\,s^{-1}}$ at early times in E1τ compared to always $\sigma_0 = 6\,\mathrm{km\,s^{-1}}$ in E1 only mildly increases the number of stars at $|z| > 1$ kpc. Model EN1τ, which differs from E1τ in lacking GMCs, has a similar thick disc, but, in common with other models without GMCs, a thin disc that is too thin. A2τ, which, like E1τ has $\sigma_0 \sim 36\,\mathrm{km\,s^{-1}}$ at early times, is as bad at providing a thick disc as A2, which has $\sigma_0 = 6\,\mathrm{km\,s^{-1}}$. It follows that choosing $\sigma_0(t)$ as in A2τ, E1τ and EN1τ has little effect on creating a thick disc.

The vertical profiles in the E models are very constant with radius (with the previously discussed exception of buckled bars), as the thick discs are set in the ICs, which by construction have radially constant vertical profiles, and the thin discs behave as in a typical Y model.

From these experiments, we conclude that the key to producing a thick disc is to put in place already at $z = 2$ a rather massive, extended and thick component. By tweaking our parameters for the IC disc or applying even higher $\sigma_0(t)$ at early times, we judge that we could eventually produce a thick disc that is compatible with the data. However, completion of this programme would not in any way *explain* the observed thick disc. This situation contrasts with the situation as regards the thin disc and the bar, which we feel are nicely explained by many of our standard models.

5.2 Varying halo density and disc mass

5.2.1 Low-density dark haloes

We now consider the impact of using a cosmologically unorthodox dark halo. In IC F, the dark halo has an anomalously large scale-length $a_{\mathrm{halo}} = 51.7$ kpc and in consequence a lower than standard density in the visible galaxy (Fig. 1). In IC G, the dark halo has only half the standard mass, so again in the star-forming galaxy the density of dark matter is smaller than cosmology implies for the MW. Reducing the halo's density at fixed disc mass favours early formation of a powerful bar. In fact, model F2 produces a bar that extends to $R \sim 10$ kpc.

As in a standard halo, a model with strong inside-out growth (F1) develops a vertical profile at $R = 8$ kpc (Fig. 15), which deviates little from an exponential, while a more compact model (F2) develops a stronger wing on its vertical density profile suggesting a thick disc.

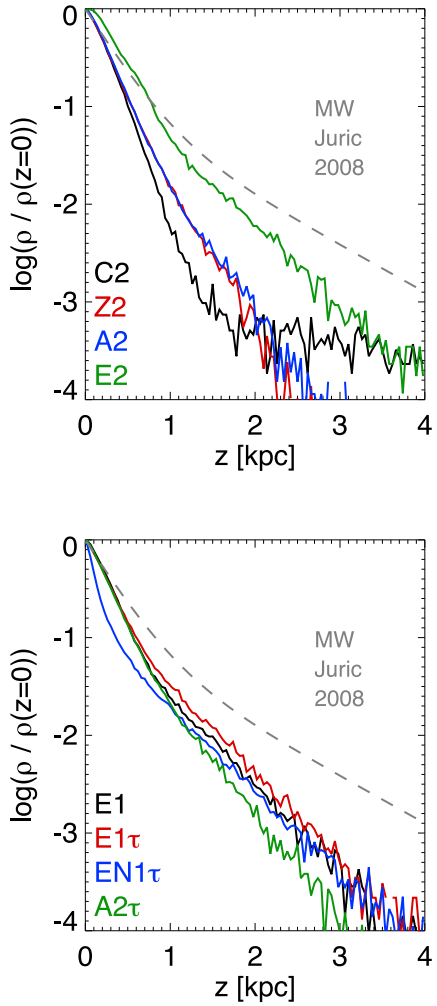

Figure 14. Vertical stellar density profiles at $R = 8$ kpc of models aimed at production of a realistic thick disc. Top: results of adding a thick disc or bulge at birth (models C2–E2). Bottom: results of modifying the way the disc is fed from the most successful IC in the top panel (E models) plus model A2τ.

Adopting the AdapLi cutoff (described at the end of Section 2.2.1) enhances the wing (F2l versus F2).

The early and powerful bar, combined with a reduced contribution to the vertical restoring force K_z from the halo, makes the disc appreciably thicker than the equivalent disc formed with a standard halo. In fact, some models, for example F2l$\zeta-$, produce discs that are thicker than that of the MW at $|z| < 2$ kpc. Unfortunately, in all our experiments a suitable thick disc, as in model F3n$\zeta-$ out to $|z| = 3$ kpc (magenta lines in Fig. 15), which has no cutoff and an enhanced supply of GMCs, is always associated with undesirable features. One is a thin disc that is too thick. Another is values of $\sigma_z(\tau)$ at $R = 8$ kpc that are too large, especially for old ages. A third is an overlong bar. On account of this long bar, $\sigma_R(\tau)$ at $R = 8$ kpc is too large, especially at young ages.

The radial density profiles of the models with low-density haloes are diverse. None resembles the distribution of added stars. Counter-intuitively, the AdapLi models (names containing 'l') are less concentrated than the standard adaptive cutoff models: AdapLi models acquire high central surface densities and powerful $m = 2$ modes early on; these modes then efficiently redistribute stars in radius.

As the amplitude A_2 quickly becomes strong in all F models, our procedure for adding stars on nearly circular orbits is questionable in these models. The particles do settle to orbits supported by the non-axisymmetric potential, but the large value of A_2 significantly distorts the radial distribution of recently introduced particles from that desired. However, large bars and strong low-m spirals are an inevitable consequence of a high baryon fraction (Sellwood & Carlberg 1984; Debattista & Sellwood 2000).

Similar to model Y4f$\zeta-$ shown in Fig. 13, the models in halo F all have vertical profiles that are considerably thicker in the outer regions of the discs compared to the inner regions. As none of the bars in these models buckles, the inner regions are always the thinnest parts of the models.

5.2.2 *Non-standard disc masses*

Finally, we briefly consider the effects of increasing or decreasing M_f, the total baryon mass. Our standard mass $M_\mathrm{f} = 5.0 \times 10^{10}\,\mathrm{M}_\odot$ is in agreement with $M_\mathrm{MW} = (5.6 \pm 1.6) \times 10^{10}\,\mathrm{M}_\odot$ determined by Piffl et al. (2014) for the MW.

Models Y1Mb+ and Y2Mb+ have M_f 50 per cent greater than standard, while Y1Mb− and Y2Mb− have M_f 40 per cent lower than standard. Increasing M_f strengthens non-axisymmetries, and vice versa when M_f is reduced. In Section 4.5, we already noted that Y2Mb− has an unusually narrow distribution of ΔL_z and in Section 4.6 we noted that Y2Mb− shows an anomalously small increase in the radial scalelength h_R with which coeval particles are distributed between addition and the final model. Both these results

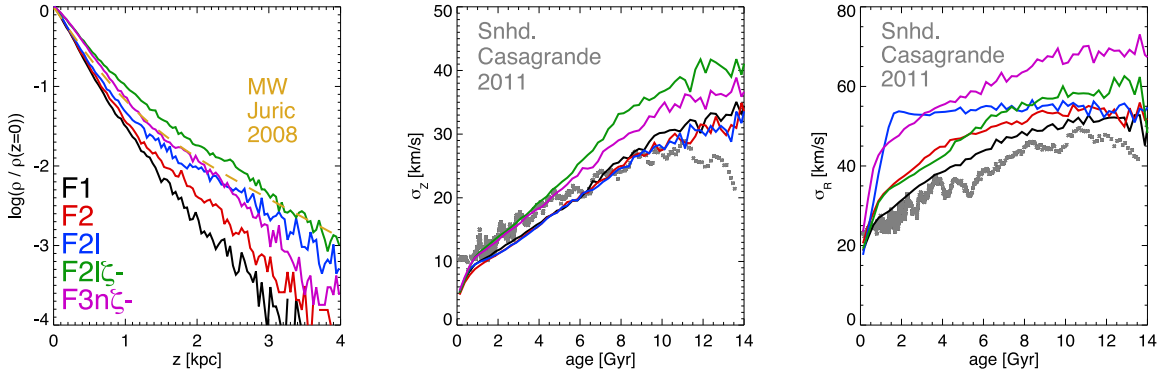

Figure 15. Characteristics at $R = 8$ kpc of models with the low-density halo F. These models develop strong bars early on, and in consequence the disc can become quite thick. Left-hand panel: vertical density profiles. Centre and right-hand panels: σ_z and σ_r as functions of age after adjustment to simulate the effects of observational uncertainties in the Snhd ages of Casagrande et al. (2011) shown as grey points.

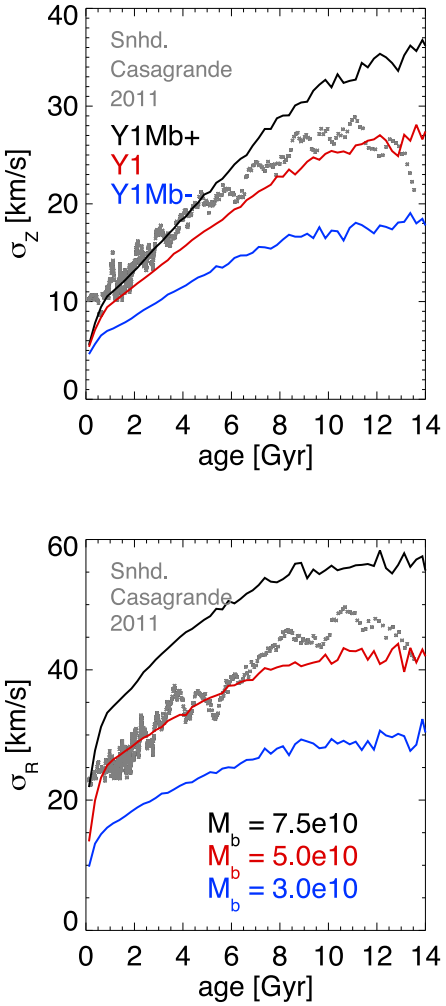

Figure 16. Velocity dispersion versus age at $R = 8$ kpc in models Y1Mb+, Y1 and Y1Mb− which differ in total final disc mass. The data have been adjusted to simulate the uncertainties and biases in the ages of Casagrande et al. (2011).

are immediate consequences of smaller departures from axisymmetry. The deleterious effect of moving from the standard value of $M_{\rm f}$ is nicely illustrated by Fig. 16: non-axisymmetries cause $\sigma_R(\tau)$ at $R = 8$ kpc to be too large at all ages in Y1Mb+ and too small at all ages in Y1Mb−. Since GMCs couple horizontal motions to vertical motions, $\sigma_z(\tau)$ at $R = 8$ kpc is always too small in Y1Mb−. In Y1Mb+, it is too large at old ages. With the standard disc mass, both $\sigma_R(\tau)$ and $\sigma_z(\tau)$ are about right.

It is worth noting that the scaleheight h_z of the disc is almost independent of $M_{\rm f}$ because increasing $M_{\rm f}$ increases both σ_z and the surface density of the disc and thus the gravitational force K_z that together with σ_z determines h_z.

These models show that our standard choices of disc and halo mass provide a balance between disc and halo gravity that is close to that present in the MW. Consequently, models Y1Mb+ and Y2Mb+ also have circular speeds at $R = 8$ kpc that are too high. To get the rotation-curve constraints right, one would have to lower the halo density, which, as we have shown above, leads to problems with overly long bars. For our standard mass values, 50 per cent of the radial force at $R = 8$ kpc already comes from the dark halo. Consequently, models Y1Mb− and Y2Mb− with lower disc masses have circular speeds that are only marginally too low. If we assume that the GMC heating in models Y1Mb+, Y1 and Y1Mb− is appropriate, the AVRs in Fig. 16 would suggest that the actual MW disc mass is slightly above $5 \times 10^{10}\,{\rm M}_\odot$ and the radial acceleration by the halo would have to be lowered mildly to account for the additional disc mass. Due to the many uncertainties involved, such as halo shape and disc mass profile, detailed estimates are not appropriate here.

6 DISCUSSION

Inevitably, our models of growing disc galaxies in live dark haloes rely on idealized assumptions. The same is true for some of the analysis presented. In this section, we discuss the impact of several of these assumptions.

For our analysis, we have used azimuthal averaging to determine mass profiles and velocity dispersions. Bars and spirals are non-axisymmetric and also defining features of galactic discs, both in observed galaxies and in our models. In the presence of a bar, stars will stream outwards at some azimuths, and inwards at others. We have computed σ_R as the standard deviation of v_R for all stars in a cylindrical shell, so any systematic radial streaming contributes to our reported values of σ_R. We hope in the near future to study the impact of the bar and spiral structure on the kinematics of discs. In such a study, the distribution of values of v_R at any point would be decomposed into its mean $\overline{v}_R$ and dispersion, and the latter would be smaller than the values σ_R reported here by $\sim\overline{v}_R^2/2\sigma_R$, which would be small for the anticipated values $\overline{v}_R \lesssim 7\,{\rm km\,s^{-1}}$.

On account of non-axisymmetric structures, perfect circular orbits do not exist in disc galaxies. However, we use the concept of an azimuthally averaged circular speed to insert star particles into our disc galaxies on near-circular orbits. Outside the bar region, this is justified by the finding that the radial velocity dispersion of young stars agrees with measurements in the Snhd, which is determined not by input σ_0 but by the local strength of non-axisymmetries. Within the bar region, we avoid inserting new stars by introducing an inner cutoff $R_{\rm cut}$. This may seem a crude assumption, but bar regions in disc galaxies are known to be deficient in SF (Sheth et al. 2002). There is plenty of SF in the central 200 pc of the MW (central molecular zone), but in our models we are not interested in these central areas of disc galaxies, which are too small to affect the large-scale dynamics studied here. Moreover, models in halo Y which set $R_{\rm cut} = 0$ do not yield results which differ significantly from those with $R_{\rm cut} > 0$.

Our models deliberately lack a model for SF from a gas component and for gas circulation including accretion and feedback, as these processes bring along both physical and numerical uncertainties of a severe nature. We find that the specifics of the setup of the initial disc and the insertion of star particles are unimportant for the outcome of our models, as long as the inserted stellar populations are sufficiently cold. We have shown that the insertion of GMCs has a much stronger effect on our models than the insertion of isothermal gas. This is because gas merely assists stars in forming spiral structure, which induces in-plane heating and radial migration. Clouds, by contrast, achieve something that neither stars nor gas can: scatter stars out of the plane and thus increase the disc's vertical scaleheight.

Although we have significantly updated the treatment of GMC populations compared to previous studies by modelling a GMC mass function, applying finite lifetimes, testing spatial clustering and having an evolving mass fraction of GMCs, our GMC particles are clearly an idealized representation of real GMCs. All our GMCs are assumed to have the same linear extent regardless of their mass,

whereas observed GMCs have sizes which on average increase with mass, and the most massive GMCs can have radii in excess of the 30 pc we adopt for the softening length of a GMC (Solomon et al. 1987). However, real GMCs are not spherical and do not have spline-kernel potentials, but are strongly substructured with most of their mass concentrated in high-density clumps (Blitz & Stark 1986). As it is unfeasible to model this small-scale structure in galaxy-wide simulations, we choose to make a simple assumption about the potential of GMCs.

Another potential lack of realism is connected to the dark halo. Although our disc grows continuously, the mass of our halo is fixed. Our Galaxy is generally believed to have had a quiet merger history since $z > 2$, and our goal is to simulate evolution since the last major merger. The inner 10 kpc of dark haloes with such quiescent formation histories are expected to have been almost completely in place by the end of the last major merger, as e.g. Wang et al. (2011b) have shown with high-resolution cosmological simulations of dark-matter-only haloes. The dark matter profiles in this region are expected to be reshaped by baryonic processes (e.g. Pontzen & Governato 2012) as they are in our simulations. In a forthcoming paper, we plan to discuss the impact on dark matter of growing discs and their bars and spirals.

Our models produce discs with single-exponential vertical profiles, whereas the disc of the MW and comparable spiral galaxies have double-exponential vertical profiles. Streich et al. (2016) recently presented observations of low-mass disc galaxies with single-exponential vertical profiles. Compared to MW mass disc galaxies, these objects are believed to have significantly lower baryon fractions (e.g. Moster, Naab & White 2013). As we have seen that thick discs in our models are connected to higher baryon fractions, the question arises whether our models in the standard halo Y on average have too low baryon fractions. At late times, there is little room to increase the mass as was shown by the high-mass models Y1Mb+ and Y2Mb+. At early times, our models have relatively high fractions of the total baryonic mass (i.e. stars and GMCs) in GMCs. The mass fraction is ∼30 per cent for a model with standard parameters such as Y1 and ∼45 per cent if ζ is lowered as in Y1$\zeta-$. Yet, these fractions are still smaller than some of the molecular gas fractions reported at redshifts $z \sim 2$ (Tacconi et al. 2010; Scoville et al. 2016). Moreover, mass-loss by stellar populations to the gas phase, which is neglected in our models, is significant over 10 Gyr, and thus old populations at 10 Gyr could contribute higher mass fractions at early times. However, a significant part (depending on the initial mass function) occurs due to core-collapse supernovae in the first 30 Myr of stellar evolution, which for our purposes is negligible. Models with higher SFRs in the beginning (e.g. Y1fs3 versus Y1f) have also been shown to not significantly change our conclusions.

Our models have the same amount of radial migration as SB09a,b, but the stars migrating outwards from the inner disc are not as hot vertically as in those models, so our models do not produce thick discs. This points towards the necessity of an additional heating source for old/inner disc populations of stars. Several possible sources, both secular and external, have been discussed in the literature: scattering of massive star-forming clumps in turbulent high-redshift galaxies (Bournaud et al. 2009), which can be regarded as an extreme form of GMC heating, the continuous decrease of birth velocity dispersion of stars in an interstellar medium which becomes less turbulent over time (Forbes et al. 2012), SF during a phase of gas-rich merger events (Brook et al. 2004) or the heating of an early thin disc by mergers (Quinn, Hernquist & Fullagar 1993).

The idealized simulations of Aumer & White (2013), in which galaxies formed from cooling gas inserted to substructured dark haloes from dark-matter-only cosmological simulations, found that, in the absence of mergers, double-exponential vertical profiles can arise in rapidly evolving young galaxies, in which the central triaxial potential first has to be restructured into an axisymmetric disc-like potential, which can host near-circular orbits. The fully cosmological hydrodynamical simulations of Aumer et al. (2013) showed that the periods of disc settling in which the thin disc can survive over cosmological time-scales typically do not start prior to $z \sim 2$. The earlier periods are characterized by mergers, high gas accretion rates and probably strong stellar feedback, which prevent stable near-circular orbits. So, from a cosmological point of view, the existence of older and hotter stellar populations is certainly plausible. As our experiments with thick-disc ICs have shown, the appearance of these objects at the start of thin-disc settling would have been less disc like than today.

7 CONCLUSIONS

We have presented a large set of controlled simulations of growing disc galaxies within non-growing, live dark haloes. Most of these models start from a thin, compact disc, with 10 per cent of the final stellar mass, but we also presented models with initially more or less massive discs, and thicker discs. We also presented a model with a bulge rather than a disc in its ICs. The models grow by the constant addition of new star particles on near-circular orbits in the mid-plane of the galaxy. At any time, particles are added according to an exponential radial density profile, but the scalelength of this profile can grow over time. The majority of our models contain a population of particles with masses in the range $10^{5-7}\,\mathrm{M}_\odot$ that represent GMCs. These particles are short-lived and have masses drawn from a power-law mass function. A subset of our models contain an isothermal gas component to represent the part of the interstellar medium that is not concentrated into GMCs. Gas is added to the isothermal component to hold roughly constant the fraction of the disc's mass that is in smooth gas.

We find the following.

(i) GMCs generate remarkably exponential vertical profiles. The scaleheight of this exponential can match that measured for the thin disc of our Galaxy providing the efficiency of SF is at the lower end of the estimated range and the masses of GMCs extend towards the upper end of the range of estimated GMC masses. These exponential profiles are very constant with radius, although buckled bars can produce deviations in the bar region.

(ii) Heating by GMCs is particularly effective early on, when the SFR is high and the stellar disc is not yet massive. GMC heating significantly delays, and in some cases can even prevent, the formation of a bar.

(iii) In order to suppress spurious two-body heating from dark matter particles to a negligible level, several millions of particles in the live dark halo are needed. For such resolutions, GMC heating is significantly more effective and even in the absence of GMCs, vertical profiles hardly change when particle numbers are increased. To resolve the vertical structures of young stellar populations, a force resolution at the sub-50 pc level is needed.

(iv) The role played by a smooth gas component is modest. It enhances the efficiency of GMCs by increasing their effective masses. It also reduces the lengths and increases the pattern speeds of bars, but only marginally.

(v) Within most models, spiral structure drives a level of radial migration within the disc that agrees well with estimates obtained by modelling the chemical composition of the Snhd.

(vi) Unless the disc has an anomalously low mass, non-axisymmetric features in the disc cause the final scalelength of the disc, h_R, to exceed the scalelength according to which particles have been added to the disc.

(vii) The disc's scaleheight h_z soon settles to a value that does not differ greatly from its final value. This is for two reasons: (i) the steady increase in the vertical velocity dispersion of a cohort of coeval stars that GMCs drive is partly offset by the disc's growing surface density, and self-gravity; (ii) freshly added stars are constantly reinforcing the density of the disc near the plane.

(viii) Models in which the scalelength for mass insertion increases more rapidly (stronger 'inside-out' growth) have weaker non-axisymmetric structures and on average shorter bars, and as a direct consequence, smaller values of σ_R/σ_z and thinner discs. By contrast, the scalelength h_R of the final disc is fairly insensitive to the rapidity with which the scalelength for insertion grows, as longer bars cause more radial redistribution.

(ix) The standard disc mass and halo parameters provide just the right level of self-gravity in the disc. Increasing the mass of the disc yields values of σ_R, σ_z and $v_{\rm circ}$ at $R = 8\,$kpc which are too high. Reducing the mass of the disc leads to unacceptably low velocity dispersions and too little radial migration. Reducing the central density of the halo leads to low $v_{\rm circ}$, to bars that arise too early and are too long, and to excessive values of σ_R at $R = 8\,$kpc.

(x) In our models, a thick disc is very hard to form. The only dynamically generated thick discs we find generate the requisite vertical velocity dispersion by $O(1)$ departures from axisymmetry that extend to $R \sim 10\,$kpc. In the case of the MW, such departures are ruled out by two facts: (i) $O(1)$ departures generate in-plane dispersions in relatively young stars that are too large, and (ii) they generally make the thin disc too thick. Moreover, in these models, the vertical profiles are significantly thicker in the outer disc than in the inner disc.

(xi) We can obtain a structure that approaches the observed thin/thick combination only by providing an essentially complete thick disc in the ICs. The requirement that the primordial thick disc (PTD) contains enough stars with the high values of the vertical action J_z that currently occur in the thick disc causes the PTD to be so extended vertically that it is not very disc-like. However, its radial extent must also be considerable because stars of the PTD do not systematically increase their guiding-centre radii: on average, they do increase their angular momenta L_z, but as the mass interior to an orbit increases, so does the value of L_z associated with a given guiding-centre radius. Hence, at $z = 2$, the PTD must already extend to $R \sim 8\,$kpc given that the thick disc extends that far now.

We are impressed that when we combine standard values for the disc mass and dark halo parameters with observationally motivated assumptions about the SFR, the mass function of GMCs and the efficiency of SF, galaxies emerge through complex dynamics that bear a striking resemblance to the MW: as functions of age, the horizontal and vertical velocity dispersions at $R = 8\,$kpc are similar to those observed, the structure of the thin disc is about right, as are the length and strength of the bar. Yet none of these quantities is prescribed by the admittedly rather arbitrary manner in which we assemble the disc: changing the disc mass, the halo density, the GMC mass function or the SFR efficiency from conventional values destroys one aspect or another of the agreement between dynamical model and observation. We consider that this outcome constitutes a significant endorsement of Λ cold dark matter cosmology and implies that our prescriptions capture many of the essential features of the physics of galaxy formation that shape disc galaxies.

Our models provide a natural explanation of the observation that the fraction of barred disc galaxies decreases with increasing redshift (Sheth et al. 2008): increasing mass renders a disc more vulnerable to bar formation both because it puts the disc more in charge of the gravitational field in which it rotates and because the effectiveness of heating by GMCs declines with the ratio of the mass of a GMC to the disc mass. In our simulations, the timing and violence of bar formation are critical for the properties of the final disc. An issue for a subsequent paper is the impact on the morphology of the bar of disc buckling after the bar has attained a critical strength.

For our models, the only way to obtain a thick disc like that of the MW appears to be to add it to the ICs. This finding suggests that the MW's thick disc was present already at $z \sim 2$ and is a relic of the time before the MW settled to its long period of secular growth. It also strongly suggests that thick-disc formation requires additional sources of heat in addition to GMCs and non-axisymmetric disc structures. The additional heat may have been provided by high-redshift mergers and/or it may have been inherited from strong turbulent motions in the early disc. In contrast, GMCs and disc structure apparently account for the full heating observed in the thin-disc population of the Snhd and thin components of external galaxies.

The MW is a more complex machine than can be adequately characterized by the standard parameters, such as h_R, $h_{z,\rm thin}$, $h_{z,\rm thick}$, $v_{\rm circ}(R)$, $\sigma_R(R)$, etc. While not as complex as the MW, our models are also too complex to be adequately characterized by a few parameters. It will be interesting to compare mock observations drawn from some of them to see whether they agree with the MW better than any naive model, and to identify residual points of conflict. For example, the circular-speed curve of the Galaxy is poorly known because the data are significantly affected by spiral structure and the bar. It will be interesting to compare with data stellar kinematics and gas line-of-sight velocities drawn from promising models. We hope to report on this exercise shortly.

ACKNOWLEDGEMENTS

We thank the referee for comments that helped improve the paper. This work was supported by the UK Science and Technology Facilities Council (STFC) through grant ST/K00106X/1 and by the European Research Council under the European Union's Seventh Framework Programme (FP7/2007-2013)/ERC grant agreement no. 321067. This work used the following compute clusters of the STFC DiRAC HPC Facility (www.dirac.ac.uk): (i) The COSMA Data Centric system at Durham University, operated by the Institute for Computational Cosmology. This equipment was funded by a BIS National E-infrastructure capital grant ST/K00042X/1, STFC capital grant ST/K00087X/1, DiRAC Operations grant ST/K003267/1 and Durham University. (ii) The DiRAC Complexity system, operated by the University of Leicester IT Services. This equipment is funded by BIS National E-Infrastructure capital grant ST/K000373/1 and STFC DiRAC Operations grant ST/K003259/1. (iii) The Oxford University Berg Cluster jointly funded by STFC, the Large Facilities Capital Fund of BIS and the University of Oxford. DiRAC is part of the National E-Infrastructure.

REFERENCES

Aumer M., Binney J. J., 2009, MNRAS, 397, 1286
Aumer M., Schönrich R., 2015, MNRAS, 454, 3166
Aumer M., White S. D. M., 2013, MNRAS, 428, 1055
Aumer M., White S. D. M., Naab T., Scannapieco C., 2013, MNRAS, 434, 3142
Aumer M., White S. D. M., Naab T., 2014, MNRAS, 441, 3679
Barbanis B., Woltjer L., 1967, ApJ, 150, 461
Beasley M. A., San Roman I., Gallart C., Sarajedini A., Aparicio A., 2015, MNRAS, 451, 3400
Bensby T., Feltzing S., Lundström I., 2003, A&A, 410, 527
Bensby T., Alves-Brito A., Oey M. S., Yong D., Meléndez J., 2011, ApJ, 735, 46
Berrier J. C., Sellwood J. A., 2015, ApJ, 799, 213
Binney J., Tremaine S., 2008, Galactic Dynamics, 2nd edn. Princeton Univ. Press, Princeton, NJ
Binney J., Gerhard O. E., Stark A. A., Bally J., Uchida K. I., 1991, MNRAS, 252, 210
Bird J. C., Kazantzidis S., Weinberg D. H., Guedes J., Callegari S., Mayer L., Madau P., 2013, ApJ, 773, 43
Bland-Hawthorn J., Cohen M., 2003, ApJ, 582, 246
Blitz L., Stark A. A., 1986, ApJ, 300, L89
Bournaud F., Elmegreen B. G., Martig M., 2009, ApJ, 707, L1
Bovy J., Rix H.-W., Liu C., Hogg D. W., Beers T. C., Lee Y. S., 2012a, ApJ, 753, 148
Bovy J., Rix H.-W., Hogg D. W., Beers T. C., Lee Y. S., Zhang L., 2012b, ApJ, 755, 115
Brook C. B., Kawata D., Gibson B. K., Freeman K. C., 2004, ApJ, 612, 894
Carlberg R. G., 1987, ApJ, 322, 59
Carlberg R. G., Sellwood J. A., 1985, ApJ, 292, 79
Casagrande L., Schönrich R., Asplund M., Cassisi S., Ramírez I., Meléndez J., Bensby T., Feltzing S., 2011, A&A, 530, A138
Cheng J. et al., 2012, ApJ, 752, 51
Colombo D. et al., 2014, ApJ, 784, 3
Combes F., Debbasch F., Friedli D., Pfenniger D., 1990, A&A, 233, 82
Comeron S. et al., 2011, ApJ, 741, 28
Debattista V. P., Sellwood J. A., 2000, ApJ, 543, 704
Dorman C. E. et al., 2015, ApJ, 803, 24
Eskridge P. B. et al., 2000, AJ, 119, 536
Forbes J., Krumholz M., Burkert A., 2012, ApJ, 754, 48
Friedli D., Benz W., Kennicutt R., 1994, ApJ, 430, 105
García L., Bronfman L., Nyman L., Dame T., Luna A., 2014, ApJS, 212, 2
Gerhard O. E., Fall S. M., 1983, MNRAS, 203, 1253
Gilmore G., Reid N., 1983, MNRAS, 202, 1025
Hayden M. R. et al., 2015, ApJ, 808, 132
Hernquist L., 1990, ApJ, 356, 359
Holmberg J., Nordström B., Andersen J., 2009, A&A, 501, 941
House E. L. et al., 2011, MNRAS, 415, 2652
Jenkins A., Binney J., 1990, MNRAS, 245, 305
Jurić M. et al., 2008, ApJ, 673, 864
Kordopatis G. et al., 2015, MNRAS, 447, 3526
Lia C., Portinari L., Carraro G., 2002, MNRAS, 330, 821
Marinacci F., Pakmor R., Springel V., 2014, MNRAS, 437, 1750
Martig M., Minchev I., Flynn C., 2014, MNRAS, 443, 2452
Martinez-Medina L. A., Pichardo B., Pérez-Villegas A., Moreno E., 2015, ApJ, 802, 109
Meidt S. E. et al., 2015, ApJ, 806, 72
Miller R. H., Smith B. F., 1979, ApJ, 227, 407
Minchev I., Famaey B., 2010, ApJ, 722, 112
Minchev I., Martig M., Streich D., Scannapieco C., de Jong R. S., Steinmetz M., 2015, ApJ, 804, L9
Moster B. P., Naab T., White S. D. M., 2013, MNRAS, 428, 3121
Murray N., 2011, ApJ, 729, 133
Nidever D. L. et al., 2014, ApJ, 796, 38
Parenago P. P., 1950, Astron. Zh., 27, 150
Piffl T. et al., 2014, MNRAS, 445, 3133
Pontzen A., Governato F., 2012, MNRAS, 421, 3464
Quinn P. J., Hernquist L., Fullagar D. P., 1993, ApJ, 403, 74
Roškar R., Debattista V. P., Loebman S. R., 2013, MNRAS, 433, 976
Rosolowsky E., 2005, PASP, 117, 1403
Saha K., Tseng Y.-H., Taam R. E., 2010, ApJ, 721, 1878
Sanders J. L., Binney J., 2015, MNRAS, 449, 3479
Scannapieco C. et al., 2012, MNRAS, 423, 1726
Schinnerer E. et al., 2013, ApJ, 779, 42
Schönrich R., Binney J., 2009a, MNRAS, 396, 203 (SB09a)
Schönrich R., Binney J., 2009b, MNRAS, 399, 1145 (SB09b)
Scoville N. et al., 2016, ApJ, 820, 83
Sellwood J. A., Binney J. J., 2002, MNRAS, 336, 785
Sellwood J. A., Carlberg R. G., 1984, ApJ, 282, 61
Sellwood J. A., Debattista V. P., 2009, MNRAS, 398, 1279
Sheth K., Vogel S. N., Regan M. W., Teuben P. J., Harris A. I., Thornley M. D., 2002, AJ, 124, 2581
Sheth K. et al., 2008, ApJ, 675, 1141
Shopbell P. L., Bland-Hawthorn J., 1998, ApJ, 493, 129
Solomon P. M., Rivolo A. R., Barrett J., Yahil A., 1987, ApJ, 319, 730
Solway M., Sellwood J. A., Schönrich R., 2012, MNRAS, 422, 1363
Sormani M. C., Binney J., Magorrian J., 2015, MNRAS, 449, 2421
Spitzer L., Jr, Schwarzschild M., 1953, ApJ, 118, 106
Springel V., 2005, MNRAS, 364, 1105
Streich D., de Jong R. S., Bailin J., Bell E. F., Holwerda B. W., Minchev I., Monachesi A., Radburn-Smith D. J., 2016, A&A, 585, A97
Strömberg G., 1946, ApJ, 104, 12
Tacconi L. J. et al., 2010, Nature, 463, 781
Toth G., Ostriker J., 1992, ApJ, 389, 5
van der Kruit P. C., Searle L., 1982, A&A, 110, 61
Velazquez H., White S. D. M., 1999, MNRAS, 304, 254
Wang J. et al., 2011a, MNRAS, 412, 1081
Wang J. et al., 2011b, MNRAS, 413, 1373
Wegg C., Gerhard O., 2013, MNRAS, 435, 1874
Widrow L. M., Dubinski J., 2005, ApJ, 631, 838
Wielen R., 1977, A&A, 60, 263
Wisnioski E. et al., 2015, ApJ, 799, 209
Xue X. X. et al., 2008, ApJ, 684, 1143
Yoachim P., Dalcanton J. J., 2006, AJ, 131, 226
Young J. S., Scoville N. Z., 1991, ARA&A, 29, 581
Yurin D., Springel V., 2014, MNRAS, 444, 62
Zhao D. H., Jing Y. P., Mo H. J., Börner G., 2009, ApJ, 707, 354

This paper has been typeset from a TEX/LATEX file prepared by the author.